arXiv:1404.0709v1 [astro-ph.EP] 2 Apr 2014

HERSCHEL EVIDENCE FOR DISK FLATTENING OR GAS DEPLETION IN TRANSITIONAL DISKS†

J. T. Keane[1], I. Pascucci[1], C. Espaillat[2], P. Woitke[3], S. Andrews[4], I. Kamp[5], W.-F. Thi[6], G. Meeus[7], W. R. F. Dent[8]

ABSTRACT

Transitional disks are protoplanetary disks characterized by reduced near- and mid-infrared emission, with respect to full disks. This characteristic spectral energy distribution indicates the presence of an optically thin inner cavity within the dust disk believed to mark the disappearance of the primordial massive disk. We present new *Herschel Space Observatory* PACS spectra of [OI] 63.18 μm for 21 transitional disks. Our survey complements the larger *Herschel* GASPS program ("Gas in Protoplanetary Systems," Dent et al. 2013) by quadrupling the number of transitional disks observed with PACS in this wavelength. [OI] 63.18 μm traces material in the outer regions of the disk, beyond the inner cavity of most transitional disks. We find that transitional disks have [OI] 63.18 μm line luminosities $\sim$ 2 times fainter than their full disk counterparts. We self consistently determine various stellar properties (e.g. bolometric luminosity, FUV excess, etc.) and disk properties (e.g. disk dust mass, etc.) that could influence the [OI] 63.18 μm line luminosity, and we find no correlations that can explain the lower [OI] 63.18 μm line luminosities in transitional disks. Using a grid of thermo-chemical protoplanetary disk models, we conclude that either transitional disks are less flared than full disks, or they possess lower gas-to-dust ratios due to a depletion of gas mass. This result suggests that transitional disks are more evolved than their full disk counterparts, possibly even at large radii.

1. Introduction

Protoplanetary disks (gas-rich dust disks around young stars) provide the raw building-blocks for solar systems. While significant progress has been made in understanding the relevant evolutionary timescales of protoplanetary disks, little is known about the physical mechanisms driving the eventual dispersal of dust and gas about these young systems (for review, see: Pascucci & Tachibana 2010). The goal of this paper is to gain insight into these dispersal processes by investigating a special type of protoplanetary disk that is thought to be in the process of losing its primordial dust disk: the transitional disks.

Transitional disks, like their full protoplanetary disk cousins, are often identified by their spectral energy distributions (SEDs). While there is significant variation in the SEDs of young star systems, transitional

[1]Lunar and Planetary Laboratory, University of Arizona, Tucson, AZ 85721, USA

[2]Department of Astronomy, Boston University, Boston, MA 02215, USA

[3]SUPA, School of Physics & Astronomy, University of St. Andrews, North Haugh, St. Andrews, KY16 9SS, UK

[4]Harvard-Smithsonian Center for Astrophysics, Cambridge, MA 02138, USA

[5]Kapteyn Astronomical Institute, Postbus 800, 9700 AV Groningen, The Netherlands

[6]Université Joseph Fourier Grenoble-1, CNRS-INSU, Institut de Planétologie et dAstrophysique (IPAG) UMR 5274, 38041 Grenoble, France

[7]Universidad Autonoma de Madrid, Dpt. Fisica Teorica, Campus Cantoblanco, 28049 Madrid, Spain

[8]ALMA SCO, Alonso de Cordova 3107, Vitacura, Santiago, Chile

†*Herschel* is an ESA space observatory with science instruments provided by European-led Principal Investigator consortia and with important participation from NASA.

disks appear as a distinct subgroup of protoplanetary disks: their SEDs show reduced near- and mid-infrared emission, with respect to full disks (Strom et al. 1989). This characteristic SED points to the presence of an optically thin inner cavity, extending from the star out to $1 \sim 20$ AU. The excavation of this cavity is believed to mark the early stages of the dispersal of the primordial, massive dust disk – whose continuous dust disk extended as close as a few stellar radii to the central star (e.g., Calvet et al. 2002; Espaillat et al. 2007). The existence of inner cavities has been directly confirmed for a few transitional disks via sensitive, high-resolution millimeter observations which detect reduced (or absent) dust emission from the inner disk, as a result of a deficit of millimeter size grains (e.g., Andrews et al. 2009; Brown et al. 2009). While transitional disks may posess dust cavities, it is known that, in most cases, these dust cavities are not devoid of gas. Transitional disks are still actively accreting (e.g., Najita et al. 2007), and various optical emission lines (e.g. CO lines, [OI] 6300 Å and 5577 Å, etc.) indicate the presence of gas within the dust cavity region - though it may be depleted (e.g. TW Hya, Gorti et al. 2011).

There are three leading hypotheses for the driving mechanism behind the formation of cavities in transitional disks: (for review, see: Espaillat et al. in prep.):

- *Dust coagulation.* As disks evolve submicron-sized dust grains coagulate into larger aggregates which have little emission at infrared wavelengths and thus reduce the disk opacity. These larger aggregates would eventually coalesce into planetesimals and planetary embryos. Since dynamical timescales increase with increasing radial distance from the central star, grain growth occurs inside-out and leads to the development of an expanding optically thin inner cavity, although the total mass of this inner disk region is not necessarily lower (e.g., Dullemond & Dominik 2005).
- *Photoevaporation.* High-energy photons from the central star can drive photoevaporative winds, particularly from the outer regions of the protoplanetary disk (beyond ∼few AU). As the viscous accretion rate drops below the photoevaporation mass loss rate, a gap opens in the disk and the inner disk viscously accretes onto the star – resulting in an inner cavity (e.g. Alexander et al. 2014). Direct irradiation of the cavity wall is expected to rapidly disperse the outer disk (Alexander et al. 2006). Photoevaporative winds have been detected for select protoplanetary disks via blueshifted (∼few km/s) [Ne II] 12.81 μm lines, which traces unbound winds within the inner $\lesssim$ 10's of AU (Pascucci & Sterzik 2009).
- *Dynamical clearing by giant planets.* Dynamical interactions between the disk and an embedded giant planet (with masses roughly equal to that of Jupiter) can open gaps within the disk (e.g., Lubow et al. 1999). Gas from the inner disk (within the planet's orbit) can continue to accrete onto the central star, while most of the gas from the outer disk (beyond the planet's orbit) accretes onto the planet, and only a small amount of gas flows past the planet into the inner disk. In addition to the physical gap created by the planet, pressure gradients setup at the outer edge of the gap can act as a dust filter - allowing only grains below a critical size to reach the inner disk, and perhaps forming an optically thin inner cavity (Rice et al. 2006).

While these different mechanisms can produce qualitatively similar SEDs, they predict distinctive differences in the distribution of disk gas. Furthermore, these different processes can, and probably do, operate simultaneously.

In this paper, we use *Herschel Space Observatory* far-infrared data to examine whether full disks and transitional disks are different in their outer disk regions, beyond 10's of AU. We use the [OI] 63.18 μm emission line and the nearby 63 μm continuum emission to trace the gas and dust components respectively, beyond 10∼100 AU (e.g. Aresu et al. 2012). In addition, we use ancillary data to characterize our sample at different wavelengths. In *Section 2*, we provide a short description of our sample, the *Herschel*/PACS observations and data reduction, and the ancillary stellar and disk properties used to characterize our sample. In *Section 3*, we summarize our [OI] 63.18 μm line 63 μm continuum results. Most notably, we find that transitional disks possess [OI] 63.18 μm line luminosities a factor of 2∼3 lower than full disks, despite having similar 63 μm continuum luminosities – a trend previously identified by Howard et al. (2013), though

expanded in this work with quadruple the number of transitional disks. In *Section 4*, we rule out various observable stellar and disk properties (e.g. FUV and X-ray luminosity) as the potential cause for this [OI] 63.18 μm line luminosity difference between full disks and transitional disks. In *Section 5* we use the results of the DENT grid (a grid of 300,000 thermo-chemical protoplanetary disk models, by Woitke et al. 2010), to examine other possible causes for the [OI] 63.18 μm line luminosity difference. We conclude that the lower [OI] 63.18 μm line luminosity of transitional disks could be due to transitional disks either being less flared, or by having lower gas-to-dust ratios. In *Section 6*, we discuss the implications of this result for disk evolution models, and potential followup observations.

2. Observations and Data Reduction

2.1. Sample Description

We selected 21 transitional disks from predominantly young (a few Myr old) and nearby ($\leq$ 200 pc) star-forming regions. Five additional transitional disks were selected from the GASPS sample ("Gas in Protoplanetary Systems," Dent et al. 2013), resulting in a total of 26 transitional disks. Our sample is listed in *Table 1*. The transitional disks were identified by significant dips in their *Spitzer*/IRS spectra. (For the relevant spectra used to identify each transitional disk as transitional, see: Brown et al. 2007; Calvet et al. 2002; Espaillat et al. 2010; Furlan et al. 2009; Kim et al. 2009; Merín et al. 2008, 2010.) Because only 10% of protoplanetary disks are transitional (e.g. Williams & Cieza 2011; Muzerolle et al. 2010) we selected targets from a number of star-forming regions, including Taurus-Auriga, Ophiuchus, Chameleon and Lupus. Targets that have been previously modeled either with continuum radiative transfer codes, or simple prescriptions for the disk inner cavity were given preference, as were objects with archival measurements of accretion rates and infrared and millimeter observations.

For comparison with our sample of transitional disks, we selected an additional 33 protoplanetary disks from the GASPS ("Gas Survey of Protoplanetary Systems," Dent et al. 2013) survey of the Taurus-Auriga star-forming region[1]. These disks were selected as being typical protoplanetary disks, with IRS spectra close to the Taurus-Auriga mean (D'Alessio et al. 2006), and were also selected to sample similar spectral types to those of the transitional disks. Like the transitional disk subsample, we took preference for objects with known accretion rates and millimeter observations. Of these 33 protoplanetary disks, 15 have jets/outflows as identified by a combination of optical and near-IR spectroscopy and imaging (see Kenyon, Gomez, & Whitney 2008, and references therein). We will refer to this subsample as "outflow" sources. The remaining 18 disks without outflows will be referred to as "full" disks. This distinction between outflow disks and full disks varies slightly from Howard et al. (2013), who identified outflow disks as objects with either directly imaged jets in Hα, [OI] λ6300, [SII] λ6371, being associated with Herbig-Haro objects, or having very broad [OI] λ6300 emission line profiles. This slight difference in definition only changes the classification of two disks (AA Tau and DL Tau). None of our full disks were noted to have broadened or spatially-extended [OI] 63.18 μm emission in Howard et al. (2013).

Targets with binary companions represent a possible source of contamination within our samples given the large spaxel size of PACS (9.4" on a side, which corresponds to a projected separation of $\sim$ 1300 AU at the distance of Taurus). Close binary companions can interact with the primary star's disk, and produce transitional SEDs (e.g. CoKu Tau/4, Ireland & Kraus 2008). Medium and large separation binaries (projected separations $>$ 10 AU) do not seem to strongly affect the first steps of planet formation (grain growth and dust settling) (Pascucci et al. 2008). However, binaries with separations $\leq$ 40 AU significantly hasten the process of disk dispersal (Kraus et al. 2012). While it might be best to remove all binaries from our sample and just focus on single stars, this approach could bias our samples and as such our results. The Taurus-Auriga star-forming region, from which we draw most of the full disks, has been well surveyed for multiplicity. However, Ophiuchus, Chameleon and the Lupus star-forming regions, from which we draw our

[1]An additional full disk, SZ 50, from the Cha I star forming region, was included in order to more properly match the spectral type distribution between full disks and transitional disks.

sample of transitional disks, have not been as well studied. Thus, there are very likely undetected multiple systems within our transitional disk sample. We opted to retain full disks within multiple systems, as long as the mid-infrared flux (~ 10 μm) ratio between members is large ($L_{IR,primary}/L_{IR,secondary} \gtrsim 3$), and the protoplanetary disks are not circumbinary. Targets that do not meet this criterion are excluded from all analysis (though they are included in tables and figures, for reference). *Table 1* lists the multiplicity status for all targets, as well as the relevant references for the projected separations and mid-infrared flux ratio for binaries.

2.2. *Herschel* PACS Spectroscopy

We obtained *Herschel Space Observatory* PACS (Poglitsch et al. 2010) spectroscopy for our sample of 21 transitional disks. The relevant *Herschel* observation identification numbers (ObsIDs), exposure times, and dates of our observations are listed in *Table 1*. The five additional transitional disks (DM Tau, LkCa 15, GM Aur, TW Hya and UX Tau), and the entire sample of full disks and outflow disks were previously observed as part of the *Herschel* Key Program: GASPS (PI, W. Dent). We used the line spectroscopy mode ("PacsLineSpec") to take spectra centered on the [OI] 63 μm line, between 62.93 and 63.43 μm. All of the observations were executed in "ChopNod" mode, in order to remove telescope emission and background.

We reduced our original observations and re-reduced the GASPS archival data with the *Herschel* Interactive Processing Environment (HIPE, Ott 2010) version 9.0.0. We used the default "ChopNodLineScan" pipeline along with the most recent calibration tree (CalTree 32). The data reduction process included: removal of saturated and overly-noisy pixels; differencing the on-source and off-source observations; spectral response function division; rebinning to the native resolution of the instrument (oversample = 2, upsample = 1); spectral flat fielding; and averaging over the two nod positions. We extracted our spectrum from the central spaxel and accounted for diffraction losses to neighboring spaxels with an aperture correction provided in HIPE. Since outflow targets generally can have extended emission, spanning multiple spaxels (Podio et al. 2012; Howard et al. 2013), our measured fluxes for these outflow targets will generally underestimate their true fluxes. We verified that for all of our transitional disks and full disks that there was no appreciable emission in neighboring spaxels. This lack of extended emission also suggests that there is no significant mispointing in the observations of our transitional disks and full disks.

2.3. Stellar and Disk Properties

To interpret our *Herschel* PACS observations of [OI] and its relationship to the protoplanetary disk environment, we aggregated stellar properties (effective temperature, bolometric luminosity, FUV and X-ray luminosities, etc.) as well as disk properties (disk mass, disk structure, accretion rates) that, through past work, are known to affect the [OI] 63.18 μm emission. In this section, we explain the methods by which we derived these stellar and disk properties. We will relate these to our *Herschel* observations in *Section 4*.

2.3.1. Effective Temperature and Bolometric Luminosity

We determined stellar effective temperatures by relating the host star's spectral type (from the literature) to the corresponding effective temperature (Luhman 1999) as listed in *Table 2*. Generally, we do not assume that the effective temperatures are accurate to more than one spectral subtype (~ 100 K).

We self-consistently derived bolometric luminosities for all targets by performing a bolometric correction on de-reddened, literature-available I-band photometry listed in *Table 2*. I-band photometry is preferential, as it is less affected by intervening dust. We de-reddened all of our I-band fluxes by relating V-band extinctions (which are more commonly reported in the literature), to I-band extinctions using relationships from Mathis (1990), assuming R_V values typical of the ISM ($R_V = 3.1$). The de-reddened continuum fluxes were converted to luminosities using the known distances to each different star-forming region (see *Table 1* and references therein). Finally, bolometric corrections from Luhman (1999) were used to calculate bolometric luminosities for each target. These effective temperatures and bolometric luminosities are listed in *Table 3*.

2.3.2. FUV Luminosities and Accretion Rates

While ultraviolet observations of T Tauri stars would provide the most direct measurement of the FUV luminosity, these observations are notoriously difficult. Instead, we made use of the well known correlation between accretion rate and FUV excess emission, to derive FUV luminosities from stellar accretion rates (e.g. Dahm 2008; Herczeg & Hillenbrand 2008). Accretion rates can be determined from a large number of other more commonly measured emission lines (e.g. Rigliaco et al. 2011).

We used the Hα emission line at 6563 Å to estimate stellar accretion rates. Hα is advantageous because is a very commonly reported observational diagnostic, and it correlates well with accretion luminosities (the excess luminosity arising from the infall and accretion of material onto the central star), as derived from other accretion tracers (e.g. Rigliaco et al. 2011). To determine accretion luminosities, we calculated the Hα line fluxes from literature Hα equivalent widths (listed in *Table 2*). For targets with multiple Hα equivalent widths available in the literature, we used the mean equivalent width[2]. To determine Hα line fluxes, we combined the Hα equivalent width with the nearest available photometric point in the literature: R-band. De-reddening was done similarly as for our bolometric luminosity analysis: using V-band extinctions converted to R-band extinctions via the relationships of Mathis (1990). The de-reddened line fluxes were converted to line luminosities using the known distances to each different star-forming region (see *Table 1* and references therein). The Hα line luminosities, $L_{H\alpha}$, were then converted into accretion luminosities, L_{acc}, with the empirical relationships of Fang et al. (2009):

$$\log\left(L_{acc}/L_{\odot}\right) = (2.27 \pm 0.23) + (1.25 \pm 0.007) \times \log\left(L_{H\alpha}/L_{\odot}\right) \quad (1)$$

Our derived accretion luminosities are listed in *Table 3*. From our accretion luminosities, we then used the empirical relationships of Yang et al. (2012) to relate accretion luminosities to FUV luminosities:

$$\log\left(L_{FUV}/L_{\odot}\right) = -1.670 + 0.836 \times \log\left(L_{acc}/L_{\odot}\right) \quad (2)$$

Our derived FUV luminosities are also listed in *Table 3*. For the 12 disks shared between this study and Yang et al. (2012), we found that our FUV luminosities agreed to those derived by Yang et al. (2012) within 0.35 dex. We found no systematic shift between our Hα-derived FUV luminosities, and their directly measured FUV luminosities. Stellar chromospheric activity can also result in Hα emission, so we used the spectral type dependent, equivalent width cutoffs of White & Basri (2003) to distinguish between chromospheric activity and accretion. For targets where the Hα equivalent width fell below these cutoffs, we report accretion and FUV luminosity upper limits.

Converting accretion luminosities to accretion rates requires some physical knowledge of the system and the processes of accretion. Gullbring et al. (1998) developed a simple magnetospheric accretion model whereby the accretion luminosity is generated by the release of potential energy as gas falls from the inner edge of the disk onto the surface of the star along stellar magnetic field lines. In this model, the accretion rate, $\dot{M}$ is related to accretion luminosity by:

$$\dot{M} = \frac{L_{acc} R_{\star}}{G M_{\star} (1 - \frac{R_{\star}}{R_{in}})} \quad (3)$$

where $R_{\star}$ and $M_{\star}$ are the radius and mass of the star, G is Newton's gravitational constant, and R_{in} is the inner truncation radius of the disk. R_{in} is generally unknown, but is usually assumed to be $\approx 5R_{\star}$, which corresponds to the typical co-rotation distance (Gullbring et al. 1998; Shu et al. 1994). The stellar radius is determined from the star's effective temperature and bolometric luminosity via the Stefan-Boltzmann Law. We used pre-main sequence evolutionary tracks from Siess, Dufour, and Forestini (2000) to relate the

[2]While Hα is known to be variable, it has been shown that the variability does not introduce significant scatter in Hα derived accretion rates (Biazzo et al. 2012). For our targets with multiple Hα equivalent widths, using either the maximum or minimum

effective temperature and bolometric luminosity to specific stellar masses. Our final accretion rates (as well as stellar masses) are listed in *Table 3*.

To test the validity of our self-consistently derived accretion rates, we compared our results with an array of other studies, including: Najita et al. (2007), Gullbring et al. (1998), Hartmann et al. (1998), White & Ghez (2001), and Hartigan, Edwards & Ghandour (1995). While differences between accretion rates can develop from several factors (including the use of different accretion tracers, different estimates of extinction, different bolometric corrections, use of non-contemporaneous photometry, etc.), we find that our accretion rates generally agree with past studies to within ∼0.5 dex. This level of variation between accretion rates computed from different tracers is typical, even if observations are contemporaneous (Rigliaco et al. 2012). Our accretion rates are also not significantly offset from past studies of accretion rates, with the exception of Hartigan, Edwards & Ghandour (1995), who find systematically higher accretion rates (although this systematic offset from other estimates has been noted in previous studies, e.g. Gullbring et al. 1998).

One of the major advantages of our study, as compared to many past studies, is that our accretion rates are self consistently derived, using all the same metric, instead of being aggregated from different literature sources which adopt different methods.

2.3.3. Disk Structure and Disk Mass

Many transitional disks in our sample have been previously modeled with radiative transfer codes in order to reproduce near- and mid-infrared disk spectra and resolved millimeter images. While the exact nature of these disk models can vary between papers, they all involve the creation of a simple, axisymmetric model disk with a prescribed dust and gas surface density. Models specific to transitional disks include gas and dust cavities within a specified radius: r_{cavity}. At the outer edge of this dust cavity, the frontally illuminated disk wall puffs up to a wall height of h_{wall}, which can significantly affect the near-infrared emission of transitional disks (both due to excess emission and shadowing of the outer disk; Espaillat et al. 2011). These disk models are then subject to simulated observations, and the relevant model spectra or resolved images are calculated (for some specified viewing angle) and fit to observations. We aggregated values for the cavity size (r_{cavity}) and the wall height (h_{wall}) from the literature. These disk properties are listed in *Table 4*. While the individual models can vary between papers, the majority of these cavity sizes and wall heights are taken from Andrews et al. (2011) and Espaillat et al. (2011), which both use similar disk models.

In addition to looking at the cavity size and wall height, we used self consistently calculated estimates of the total disk mass, from 1.3 mm and 850 μm photometry available in the literature. Following Beckwith et al. (1990), it is possible to invert observed millimeter flux into an apparent disk dust mass if we assume that the emission is (1) optically thin, (2) arises from an isothermal region of the disk, of known temperature, and (3) is due to material with a known opacity. (See Beckwith et al. 1990 and Mohanty et al. 2013 for a more detailed explanation of this process, and the assumed dust temperatures and dust opacities.) Using the canonical gas-to-dust ratio of 100-to-1, we then converted dust masses into total gas masses. The resulting total disk masses are listed in *Table 4*. It is important to note that even if we disregard uncertainties in the dust temperature or opacity and the questionable gas-to-dust ratio, these disk masses are likely lower limits. Millimeter observations are only sensitive to small dust grains, less than $\sim$ 1 cm in size. It is possible that substantial mass may be in larger grains, planetesimals or even protoplanets.

3. Results: Detection of [OI] 63.18 μm and o-H_2O Emission

We detect [OI] 63.18 μm emission from 17 of our 21 transitional disks. Coupling these new results with our reanalysis of select disks from the GASPS sample (Dent et al. 2013; Howard et al. 2013), we report [OI] 63.18 μm emission from 21 of 26 transitional disks, 12 of 18 full disks, and emission from all of the outflow disks. We fit all observed emission lines to Gaussians using an original MATLAB fitting routine. To mitigate

Hα equivalent width changes the resulting accretion rate on average only 0.12 dex. This variation is less than the uncertainty that results from the empirical relationships used to convert Hα luminosity to accretion luminosity (Fang et al. 2009).

noise in the PACS spectrum, we fit the lines over a range of wavelength baselines (the minimum wavelength range: 63.13 - 63.23 μm; the maximum wavelength range spanned the entire PACS spectrum: 62.93 - 63.43 μm). The best-fitting spectrum was deemed as the spectrum closest to the median of all line fits for a given target. The line flux of this best-fitting spectrum was calculated from the (continuum-subtracted) Gaussian line profile ($flux = amplitude \cdot \sigma_{Gaussian}\sqrt{2\pi}$). For [OI] 63.18 μm non-detections, we derive 3σ upper limits assuming a Gaussian profile with a $3\sigma_{RMS}$ peak height (where σ_{RMS} is the standard deviation of the continuum linear-fit) , and a 98 km/s line width corresponding to the FWHM of an unresolved line in PACS (*PACS Observer's Manual*). Continuum fluxes at 63 μm were also found from the best fitting Gaussian line profile: as the constant baseline flux term. Continuum emission at 63 μm was detected for all targets, with the exception of DS Tau (an upper limit of 0.037 Jy). The [OI] 63 μm line fluxes and 63 μm continuum fluxes are reported in *Table 5*, and the spectra are provided in the appendix. To validate our data reduction, we compared our resulting [OI] 63 μm line fluxes and 63 μm continuum fluxes to the fluxes reported by Howard et al. (2013). Despite using a more recent version of HIPE (version 9, rather than version 4), our fluxes generally agree with those of Howard et al. (2013) to within $\sim$ 30%, which is comparable to the absolute flux accuracy of PACS (which has a peak-to-peak accuracy $\backsim$ 30%, and RMS accuracy of $\backsim$ 10%; *PACS Observer's Manual*). Compared to this pipeline uncertainty, the uncertainties in our line fits are negligible. Representative error bars for both of these types of flux calibration uncertainty are shown in *Figure 1a* and *Figure 1b*.

Typical line fluxes (normalized to the distance of the Taurus-Auriga star-forming region, at 140 pc) are on order $10^{-16} \backsim 10^{-17}$ W/m^2, corresponding to line luminosity of $10^{-7} \backsim 10^{-5} L_{\odot}$. Continuum fluxes (again, normalized to 140 pc) range from $0.1 - 100$ Jy, corresponding to continuum luminosities ($L_{continuum} = f_{\nu}\nu 4\pi d^2$) of $10^{-2} \backsim 1\ L_{\odot}$. *Figure 1a* shows the [OI] 63.18 μm line luminosity as a function of 63 μm continuum luminosity for all of our targets. *Figure 1b* shows the ratio of [OI] 63.18 μm line luminosity to 63 μm continuum luminosity as a function of 63 μm continuum luminosity for all of our targets.

We used the Astronomy SURVival package (ASURV, LaValley, Isobe, & Feigelson 1992) to perform linear regressions and correlation tests between the line and continuum luminosities for each subsample. ASURV is particularly useful as it allows for the incorporation of censored data points (i.e. non-detection, line flux upper limits). Compared to the other subsamples, we oversample G-type stars in transitional disks (5 G-type transitional disks; 1 G-type full disk; 0 G-type outflow disks). Because of this oversampling and the seemingly chaotic nature of the G-type line and continuum fluxes, we have omitted them from many of our statistical tests[3]. Additionally, as discussed in *Section 2.1*, we also exclude multiple systems where the multiplicity likely strongly affects our *Herschel*/PACS observations. *Tables 6*, *7*, and *8* summarize the results from a variety of statistics and fitting routines that were used to characterize differences between the three subsamples. There are a number of important trends in our [OI] 63.18 μm line and 63 μm continuum luminosity data:

- [OI] 63.18 μm line luminosities are positively correlated with 63 μm continuum luminosities, both for the sample as a whole, and for each individual subsample, as shown in *Table 6*. This correlation was previously recognized in the *Herschel*/PACS GASPS survey of Taurus-Auriga protoplanetary disks (Howard et al. 2013) and Herbig Ae/Be stars (Meeus et al. 2012), though our study extends this result to a significantly larger sample of transitional disks.

- Outflow disks tend to have [OI] 63.18 μm line luminosities and 63.18 μm continuum luminosities that differ markedly from full disks and transitional disks. This is simply demonstrated in *Table 7*, which shows that both the line and continuum luminosities of outflow disks are not likely from the same parent population as either the full disks or transitional disks. As shown in *Table 8*, outflow disks tend

[3]Our oversampling of G-type transitional disks is not intentional. Due to the rarity of transitional disks we cannot discriminate transitional disks by spectral type in order to populate our transitional disk subsample. Simultaneously, it is difficult to populate subsamples of full or outflow disks with G-type stars from the GASPS Taurus-Auriga survey, since Taurus-Auriga is a low-mass star-forming region.

to have higher [OI] 63.18 μm line luminosities (by 0.5$\backsim$1 dex), higher 63 μm continuum luminosities (by $\backsim$0.5 dex), and higher line-to-continuum luminosity ratios (by $\backsim$0.5 dex). This was previously recognized by Podio et al. (2012) and Howard et al. (2013).

- Full disks and transitional disks have similar 63 μm continuum luminosities. This is most easily shown in *Table 7*, which shows that the 63 μm continuum luminosities of transitional disks and full disks are effectively indistinguishable.

- Given the same 63.18 μm continuum luminosity, full disks tend to have larger [OI] 63.18 μm line luminosities than transitional disks[4], by a factor of $\backsim$2. While this is visually evident in *Figure 1a*, there is sufficient scatter (and non-detections) to make this difficulty to quantify and the ASURV statistical tests point to indistinguishable line luminosities between the two subsamples (see *Table 7* and *Table 8*). However, this difference between full disks and transitional disks becomes clear when we examine the ratio of the [OI] 63.18 μm line luminosity to the 63 μm continuum luminosity, as shown in *Figure 1b*. The ASURV statistical tests indicate that the distribution of line-to-continuum ratios of transitional disks is significantly different from that of full disks (see *Table 7* and *Table 8*) with full disks having line-to-continuum ratios larger by a factor of $\backsim$2.

  Additionally, the best-fit linear regressions *in the line luminosity* for full disks and transitional disks, as shown in *Table 6*, are distinct. Transitional disks have steeper best-fit slopes and shallower best-fit intercepts than full disks; both of these effects contribute to larger differences in line luminosity at the relevant continuum luminosities. We checked our ASURV fit results with an alternative Bayesian metric (linmix_err.pro; Kelly 2007), and found similar differences between transitional disks and full disks.

  This difference between full disks and transitional disks was previously recognized by Howard et al. (2013) for the GASPS Taurus-Auriga sample only. Our data extends this trend to a much larger sample of transitional disks, suggesting that this lower [OI] 63.18 μm line emission is a characteristic property of transitional disks.

- There is a weak trend for M-type stars to have lower line and continuum luminosities than K-type stars. This trend is most evident in our sample of transitional disks.

Generally, the [OI] 63.18 μm line is spectrally unresolved. Most FWHM are within $\backsim$11 km/s (the native resolution of PACS) of the expected line width for an unresolved line for PACS ($\backsim$98 km/s at 60μm). This result was expected, since [OI] emission originates far out in the disk, $\backsim$AU from the central star (Woitke et al. 2010). For gas orbiting a Sun-like star, Keplerian velocities go as $V_{Keplerian} = 30km/s \cdot (a/AU)^{-\frac{1}{2}}$. Thus, beyond $\backsim$AU from the central star, we expect line widths on order $\backsim$10's of km/s. Even at these distances, Keplerian velocities dominate over thermal velocities ($\sim$ 1 km/s, assuming typical OI 63.18 μm gas temperatures of $\sim$ 100 K, Aresu et al. 2012), or turbulent velocities ($\sim$ 1 km/s, Hughes et al. 2011), and are the cause of most of the line broadening. A few objects, all outflow sources, have broader line widths, as high as 170 km/s (e.g RW Aur). In these sources, [OI] 63.18 μm emission is thought to originate from shocks along the jet and/or UV-heated gas in the outflow cavity walls (Podio et al. 2012). Line widths of $\backsim$100's of km/s reflect the similarly large shock velocities. Outflow disks can also have spatially extended [OI] 63.18 μm emission associated with the jet, which is detectable in non-central PACS spaxels (Podio et al. 2012). We verified that [OI] 63.18 μm emission was localized only in the central spaxel for our transitional and full disks. For outflow disks, we only report [OI] 63.18 μm line and 63 μm continuum fluxes from the central spaxel (for more accurate line and continuum fluxes of outflow disks, including neighboring spaxels, see Podio et al. 2012).

Our PACS spectral range fortuitously also includes the considerably fainter o-H_2O 63.32 μm emission

[4]The one notable exception is BP Tau (C2). BP Tau has a significantly lower [OI] 63.18 μm line luminosity, compared to other full disks.

line. We confirmed the detection o-H_2O emission in 5 full disks and outflow disks, previously identified by Riviere-Marichalar et al. (2012). In addition, we report the marginal detections of o-H_2O in IQ Tau, DK Tau, and BP Tau - for which Riviere-Marichalar et al. (2012) previously identified 3σ upper limits. These new detections, from the same observational data, are made possible with our updated version of the Herschel HIPE pipeline and a different line-fitting algorithm. In addition to these objects, we also report the detection of o-H_2O emission from RW Aur (observed by the GASPS survey, but not included in Riviere-Marichalar et al. 2012), and the first detection of o-H_2O 63.32 μm emission from a transitional disk: DoAr44 (original to this study). o-H_2O line fluxes and 3σ upper limits for all targets are reported in *Table 5*.

4. Trends with Observable Stellar and Disk Properties

In this section, we compare our [OI] 63.18 μm line flux results with stellar and disk properties summarized in *Section 2.3* in order to identify the origin of the trends described in the previous section. We performed correlation tests between [OI] 63.18 μm and all of these disk/star parameters using the Astronomy SURVival package (ASURV, LaValley, Isobe, & Feigelson 1992). *Tables 6*, *7*, and *8* summarize the results of these correlation tests.

4.1. Effective Temperature and Bolometric Luminosity

Since the [OI] 63.18 μm line is generally optically thick (e.g. Aresu et al. 2012), it would be expected that the line flux might increase for increasing stellar effective temperature. Similarly, one might expect that the bolometric luminosity of the host star may affect the line flux. As shown in *Table 6*, we indeed find a correlation between [OI] 63.18 μm line flux and the effective temperature and bolometric luminosity of the host star for transitional disks. We also find a correlation between the 63.18 μm continuum flux and the effective temperature and bolometric luminosity. Curiously, we do not find either of these correlations for our sample of full disks. This may be a result of the smaller span of effective temperature and bolometric luminosity covered by full disks, compared to transitional disks.

The observed correlations between bolometric luminosity and effective temperature with [OI] 63.18 μm line flux and 63.18 μm continuum flux in our transitional disk sample are expected on the basis that both the line and continuum emission are expected to be optically thick, and thus sensitive primarily to the disk temperature. This explains why the line and continuum emission are correlated with each other, as they both increase with increasing temperature. This correlation (though weaker) was also observed by Meeus et al. (2012), for their smaller sample of Herbig Ae/Be stars. This relationship is visually evident in *Figure 1a*, where the symbol of each data point is representative of the star's spectral type; generally cooler, M-type stars have lower line and continuum fluxes than K-type stars. What is more important, however, is that the effective temperatures and bolometric luminosities between full disks and transitional disks are not statistically different, as illustrated in *Tables 7* and *8*. This similarity was expected since we attempted to uniformly sample across spectral types within each subsample. This suggests that the effective temperature and bolometric luminosity alone are not enough to explain why full disks have systematically larger [OI] 63.18 μm line fluxes than transitional disks.

4.2. FUV Luminosities and Accretion Rates

Pinte et al. (2010) used disk thermo-chemical models and showed that far-ultraviolet (FUV) radiation can be a significant gas-heating mechanism, and can promote [OI] 63.18 μm line emission. For low mass stars, where chromospheric FUV is negligible, most of the FUV luminosity is generated from the infall of disk material onto the central star. This accretion process shocks and superheats the gas, generating FUV emission, which can then heat the surface layers of the surrounding disk. Indeed, we find a correlation between FUV[5] and both [OI] 63.18 μm line emission and 63.18 μm continuum emission in *Table 6*. However, for our sample, we find that transitional and full disks have statistically indistinguishable FUV[5] luminosities,

[5] L_{FUV} is directly related to L_{acc} via *Eq. 1* and *Eq. 2*, so statistical tests for the two are identical. In all Tables we only list L_{acc}.

as shown in *Tables 7* and *8*. Thus, FUV cannot be responsible for the [OI] line flux differences between full and transitional disks.

The literature is not conclusive about any accretion rate difference between transitional disks and full disks. Some studies find that transitional disks have accretion rates an order of magnitude lower than full disks (Najita et al. 2007; Espaillat et al. 2012; Kim et al. 2013). However, when the two samples are drawn from the same spectral type distribution, and the accretion rates are self-consistently derived (and not drawn from the literature), as in our study, no differences are found (Fang et al. 2009). This is illustrated in *Tables 7* and *8*.

4.3. X-ray Luminosities

More recent thermo-chemical disk models by Aresu et al. (2012, 2014) have included the effects of irradiation from stellar X-rays. Aresu et al. (2012) found that X-ray irradiation tends to become a significant driver for the [OI] 63.18 μm line emission only when $L_X > 10^{30}$ erg/s. Below this limit, FUV irradiation dominates. As shown in *Table 6* we find no correlation between L_X and either [OI] 63.18 μm line luminosity or 63 μm continuum luminosity. We also find that full disks and transitional disks have statistically indistinguishable X-ray luminosities, as shown in *Tables 7* and *8*. Furthermore, the observed X-ray luminosities are generally lower than the 10^{30} erg/s limit suggested by Aresu et al. (2012), suggesting that X-ray irradiation is not the driving mechanism for the trends between [OI] 63.18 μm line luminosity in full disks and transitional disks. Newer models by Meijerink et al. (2012) and Aresu et al. (2012) have predicted a correlation between [OI] 63.18 μm line luminosity and the *sum* of the X-ray luminosity and FUV luminosity, although this trend is not found in either the GASPS Taurus sample (Aresu et al. 2014), or in our larger sample of transitional disks.

While X-rays may not be important for the differences between subsamples, X-ray irradiation may be important for a few of the G-type stars. As noted previously, the G-type stars in our sample tend to have line and continuum fluxes that differ significantly from our other targets. Many of these G-type outliers (e.g. CHX 22, CHX 7, YLW8) have X-ray luminosities at or above the 10^{30} erg/s L_X limit of Aresu et al. (2012).

4.4. Disk Structure and Disk Mass

Is the lower [OI] 63.18 μm line luminosity in transitional disks simply due to the *lack* of gas in the inner cavity of transitional disks? Kamp et al. (2010) showed for a small number of thermo-chemical disk models that creating an inner cavity (out to 10 AU) *completely devoid of gas*, decreased the [OI] 63.18 μm line flux by a factor of 1.5. Bruderer (2013) has shown that even though most [OI] emission originates from the outer disk (beyond 10's of AU), depleting gas within the inner cavity of transitional disks can reduce the disk's total [OI] 63.18 μm luminosity by factors of up to several. Given the large beam of *Herschel*/PACS ($\sim$ 1000's of AU, at the distance of Taurus), a reduction in the [OI] 63.18 μm line flux by a factor of ~ 2 as we observe would require a depletion of gas in the inner disk by a factor $\gtrsim 100$ (see Fig. 18 of Bruderer 2013). These scenarios proposed by Kamp et al. (2010) and Bruderer (2013) seem unlikely in view of our finding that the mass accretion rates of transitional disks in our sample are statistically indistinguishable from those of full disks in Taurus.

One might expect that the heating of the gas, and by extension the luminosity of the [OI] 63.18 μm line, is affected by the distribution of the dust, hence a correlation between the dust cavity size or wall height and the [OI] 63.18 μm line. We find no correlation between the cavity sizes or wall heights of transitional disks and either the [OI] 63.18 μm line luminosites or 63.18 μm continuum luminosities. This result is shown in *Table 6* and graphically in *Figure 2*. This suggests that either [OI] 63.18 μm is tracing material well beyond the inner cavity and/or the distribution of gas in the inner cavities of full disks and transitional disks is similar. While this result is suggestive, more work following Kamp et al. (2010) and Bruderer (2013) needs to be done to determine the relationship between the size of transitional disk cavities, the gas-to-dust ratio in these cavities, and [OI] 63.18 μm emission.

Finally, we find that the disk dust masses for full and transitional disks are statistically indistinguishable,

and that there is no correlation with the dust mass and either the [OI] 63.18 μm line luminosities or 63 μm continuum luminosities. This is expected, given that both the [OI] 63.18 μm line and 63 μm continuum emission are mostly optically thick.

5. Trends with Model-Derived Disk Properties

Thus far, we have been unable to satisfactorily explain the difference in [OI] 63.18 μm line flux between full and transitional disks. To identify other possible causes for the trends we used the DENT ("Disk Evolution with Neat Theory") grid of themo-chemical models by Woitke et al. (2010) to look for correlations between [OI] 63.18 μm line emission and various disk properties, that are not directly observable. Of the free parameters in the DENT grid (e.g. column density, disk inner/outer radius, grain sizes, inclination, etc.), there are only two parameters that can cause the observed [OI] 63.18 μm line flux trends: disk flaring, and the disk gas-to-dust ratio.

To illustrate trends within the DENT grid, we have developed a novel approach for analyzing the large suite of DENT disk models (totaling over 300,000 unique disks). *Figure 3* illustrates an example of this technique, for the case where we investigate how [OI] 63.18 μm line and 63.18 μm continuum emission change as a function of FUV excess luminosity (which is discussed previously, in *section 4.2*). Using an original MATLAB script, we select a randomized subsample of a few thousand[6] unique disk models from the full DENT grid. Generally, we constrain this randomized subsample to consist of low mass stars (M- and K-type), similar to our sample of transitional and full disks. Next, for each of the selected disk models, we search the full DENT grid for all of the disk models that possess identical stellar/disk properties, *except* for the quantity that we are interested in – FUV excess in this case. Since the DENT grid allows for two different FUV excesses (0.001 and 0.1 L_{star}), this results in a few thousand emphpairs[7] of disks.

From this ensemble of disk model pairs, we can perform a number of analyses. *Figure 3a* shows the ensemble of disk models in a plot of [OI] 63.18 μm line flux vs. 63.18 μm continuum flux[8] , similar to *Figure 1a*. In this plot, each of the disk models is represented by a colored point, with the color corresponding to its FUV excess. The vectors connect individual disk pairs. These vectors can be thought of as "evolutionary tracks" which show how one disk would change if the FUV excess changed (in this case, the arrow points in the direction of increasing FUV excess). Due to the extreme number of disk models in the DENT grid, even the randomized subsample in *Figure 3a* is dense and difficult to interpret. To simplify interpretation, *Figure 3b* displays two contour intervals – one for each FUV excess – indicating the region that contains 67% of the disk models for that particular FUV excess. These contours are generated by binning the data in both continuum flux and line flux space (usually with bins 0.25 dex in size). A small number of "evolutionary tracks" are included, to reinforce the concept that we are tracking disk models as a particular quantity is changed. Lastly, *Figure 3c* illustrates the *mean* "evolutionary track" for all of our disk pairs. To generate this figure, we take each pair and calculate the *change* (signified by a "Δ" in the figure axes) in continuum flux and *change* in line flux between each pair member. The vector displayed represents the mean change in continuum and line flux for our entire ensemble of disk pairs. The error bars indicate the 1-σ variations in this single step-up in FUV excess. This last figure, *Figure 3c* is particularly useful, as it shows information that is easily lost in the large apparent scatter in *Figure 3a* and *Figure 3b*. For example, while it is clear in these other figures that increasing the FUV excess increases the line flux, it is not as obvious how much this line flux changes, and the relative uncertainties. It's also not obvious in the other figures that the change in continuum flux is so consistent (represented by the very small horizontal error bars) between all

[6] in general, our results are not sensitive to the number of disk models selected, as long as it is fairly large ($\gtrsim$ 100).

[7] For other stellar/disk parameters where more than two values are possible, we form sets containing the same number of disk models as the number of possible values for that stellar/disk parameter. For example, there are five possible gas-to-dust ratios within the DENT grid; thus when performing our analysis for gas-to-dust ratios, we form several thousand sets of disk models, each containing five disks that are identical with the exception of their gas-to-dust ratios.

[8] It is not possible to exactly duplicate *Figure 1a* with the DENT grid, as the DENT grid does not include a 63 μm photometric

the DENT models. In the following sections, we will make use of figures similar to *Figure 3b* and *Figure 3c* to investigate how changing various stellar/disk parameters affect the observed [OI] 63.18 μm line fluxes and 63.18 μm continuum fluxes.

5.1. Disk Flaring

One of the early predicted trends of the DENT grid was that [OI] 63.18 μm emission may trace the flaring of the disk (Woitke et al. 2010). In a flared disk, the disk surface is directly illuminated by the central star, causing higher temperatures and stronger [OI] 63.18 μm emission. Within the DENT model grid, geometric flaring of the gas disk is parameterized[9] by the value of β: the disk scale height, h, as a function of radial distance, r, can be described by:

$$h(r) = h_0 \left(\frac{r}{r_0}\right)^{\beta} \tag{4}$$

where h_0 is the disc scale height (fixed at 10 AU), and r_0 is a fixed reference distanced (fixed at 100 AU). In the DENT grid, there are three possible flaring parameters, $\beta = 0.8$, $\beta = 1.0$, and $\beta = 1.2$. A flaring parameter as low as $\beta = 0.8$ is more appropriate for the late stages of disk evolution (e.g. debris disks), and not for our study of young protoplanetary disks (Kamp et al. 2011). Thus, we have excluded models with $\beta = 0.8$ from our analysis. It is important to note that when we refer to "flaring," we are referring to the flaring of the *gas* disk. In the DENT grid, the dust is either well mixed with the gas, or settled. The dust disk scale height, h_{dust}, is parameterized as:

$$h_{dust}(r, a) \propto h(r) a^{-s/2} \tag{5}$$

where h is the gas scale height (*Eq. 4*), a is the grain size, and s describes the strength of dust settling: $s = 0$ for a well-mixed disk, and $s = 0.5$ for a settled disk. We find that within the DENT grid, there is no *systematic* difference between the [OI] 63.18 μm line luminosity of disks with either well-mixed or settled dust disks. Settled dust disks do have systematically lower 63 μm continuum luminosities than well-mixed disks, by ~ 0.7 dex. Instead, we focus on the effects of changing the flaring of the gas disk.

Figure 4 illustrates how the [OI] 63.18 μm line luminosity and 63 μm continuum luminosity change as disks become more flared according to the DENT grid. From *Figure 4*, we can see that increasing the disk flaring from $\beta = 1.0$ to $\beta = 1.2$ can increase the [OI] 63.18 μm line luminosity by ~ 0.5 dex, while not significantly altering the 63 μm continuum luminosity. This increase in flaring in the DENT grid results in generally warmer gas in the disk surface, resulting in larger [OI] 63.18 μm line luminosities. Since changing the flaring of the disks only changes the [OI] 63.18 μm line luminosity, and not the 63 μm continuum luminosity, this may provide a natural explanation for the decreased [OI] 63.18 μm line luminosity in transitional disks compared to full disks. This would imply that transitional disks are *less* flared than full disks, and that their lower [OI] 63.18 μm line luminosities are the result of cooler disk gas surface layers. If the gas in transitional disks is indeed cooler than in full disks, this might be linked to the reduction or removal of some gas heating mechanism. Aikawa & Nomura (2006) have shown that growth and settling of larger dust grains ($\sim$ 10 cm in diameter) leads to decreased photoelectric heating in the disk atmosphere and less disk flaring. However, these large dust grains will quickly settle towards the disk midplane, resulting in reduced far-infrared emission, which we do not see in our sample. An alternative explanation could be that the stellar FUV photons responsible for heating the [OI] emitting disk surface layers (Aresu et al. 2012) are being absorbed at a vertically extended dust inner rim. Future SED modeling may be able to disentangle these two possibilities.

point. Instead, we used the 65 μm photometric point as a proxy. For most DENT models, there is not a significant change in the continuum luminosity between 60, 65 or 70 μm.

[9] In principle, the vertical scale height of the gas disk should be self-consistently derived from hydrostatic equilibrium, given the temperature structure of the disk. This is *not* done in the DENT grid. Using parameterized disk structures allows for a

5.2. Disk Gas-to-Dust Ratio

A second, though less well recognized trend in the DENT grid is that [OI] 63.18 μm emission may trace the disk gas-to-dust ratio. From *Herschel*/PACS and millimeters observations combined with dust and gas modeling, Thi et al. (2010) suggested that the transitional disk TW Hya possess a lower gas-to-dust ratio than the standard interstellar value of 100, though this suggestion has been disputed in recent years (Gorti et al. 2011; Bergin et al. 2013). Meeus et al. (2012) has also suggested, from analysis of the DENT grid, that variations in the [OI] 63.18 μm line luminosities of Ae/Be stars, could be a result of variations in the gas-to-dust ratio, although they do not explore this further.

Figures 5 and *6* illustrate how the [OI] 63.18 μm line luminosity and 63 μm continuum luminosity change as the gas-to-dust ratio changes within the DENT grid. We consider two scenarios: first the effects of changing the gas-to-dust ratio while holding the *dust* mass constant, as shown in *Figure 5*; and second, the effects of changing the gas-to-dust ratio while holding the *gas* mass constant, as shown in *Figure 6*. It is necessary to consider these two scenarios independently since identical gas-to-dust ratios can be constructed from different combinations of gas and dust mass.

As shown in *Figure 5*, increasing the gas-to-dust ratio, *while holding the dust mass constant* (in other words: we are increasing the gas-to-dust ratio by adding gas), results in increased [OI] 63.18 μm line luminosities. The increase in line luminosity is greatest for low dust masses: where changing the dust to gas ratio from 10^{1} to 10^{-3} results in an increase in line luminosity of ~ 2 dex. At higher dust masses, the increase in line luminosity across the same range of gas-to-dust ratio results in an increase in line luminosity of ~ 1 dex. Since the [OI] 63.18 μm line is generally optically thick (e.g. Aresu et al. 2012), the increase in line luminosity with increasing gas mass is likely due to an increased heating rate, perhaps by H_2 photo-dissociation, collisional de-excitation of H_2^*, or photo-electric heating (e.g. Woitke et al. 2009). From *Figure 5*, it is also clear that changing the gas-to-dust ratio, while holding the dust mass constant, does not change the 63 μm continuum luminosity. This is not unexpected, since the continuum luminosity is tracing the dust in the disk, which in these cases, remains unchanged.

Figure 6 shows the complicated effects of increasing the gas-to-dust ratio, *while holding the gas mass constant* (in other words: we are increasing the gas-to-dust ratio by removing dust). In general, increasing the gas-to-dust ratio by removing dust significantly decreases the 63 μm continuum luminosity by $0.2 \sim 2$ dex, depending on the gas mass. The behavior of the [OI] 63.18 μm line luminosity as the gas-to-dust ratio changes, while holding the gas mass constant, is even more complicated. For gas masses below $10^{-6}\,M_{\odot}$, the [OI] line luminosity decreases, with increasing gas-to-dust ratio. For gas masses above $10^{-6}\,M_{\odot}$, the [OI] line luminosity increases, with increasing gas-to-dust ratio - although the rate of this increase decreases with decreasing dust mass. This decrease in [OI] line luminosity with decreasing dust mass may indicate the signifcance of dust-driven heating processes within the disk, such as PAH heating and collisional heating (e.g. Woitke et al. 2009).

So, could the lower [OI] 63.18 μm line luminosities of transitional disks be explained by changes in the gas-to-dust ratio? Given the two ways of changing the gas-to-dust ratio, the simplest possible explanation is that transitional disks have lower gas-to-dust ratios, *by having less gas mass* than full disks. As shown in *Figure 5*, a decrease of gas-to-dust ratio of only ~ 0.5 dex would be able to explain the factor of $\sim$ few lower [OI] 63.18 μm line luminosities in transitional disks, while retaining similar 63 μm continuum luminosities. While there may be specific evolutionary pathways whereby increasing the dust mass can also explain the factor of $\sim$ few lower [OI] 63.18 μm line luminosities in transitional disks, changes in the dust mass strongly affect the 63 μm continuum luminosities, as shown in *Figure 6*. Furthermore, our estimates of dust mass from millimeter observations (see *Section 4.4*), suggest that there is no statistical difference between the dust masses of full and transitional disks.

BP Tau may be an example of a more evolved full disk that is dispersing its gas, and decreasing its

wider, unbiased exploration of disk parameter space - while still assessing the relative influence of key parameters on observable quantities. See *Section 2* of Kamp et al. (2011) for a discussion of the parameterized approach.

gas-to-dust ratio. Dutrey et al. (2003) showed that BP Tau is anomalous in many regards: its CO and dust disk are small and faint; the ^{12}CO $J = 2 \rightarrow 1$ transitional is optically thin; and that with respect to the dust, the CO is depleted by a large factor (~ 100). One possible explanation discussed by Dutrey et al. (2003) is that BP Tau may be depleted in gas with respect to dust, and have a lower gas-to-dust ratio than other full disks. As shown in *Figure 1a*, BP Tau has an anomalously low [OI] 63.18 μm line luminosity compared to other full disks. This result confirms that BP Tau is indeed different from other full disks. Furthermore, the low [OI] 63.18 μm line luminosity is consistent with the hypothesis of Dutrey et al. (2003), that BP Tau has a lower gas-to-dust ratio than typical full disks, by ~ 1 dex.

6. Discussion

6.1. Implications for Disk Evolution Models

Photoevaporation may be a natural mechanism by which the disk gas-to-dust mass ratio is reduced with time. High-energy stellar photons heat the disk and drive a photoevaporative wind which primarily removes the gas component from the disk surface. Amongst our sample of transitional disks, CS Cha, TW Hya, T Cha, RXJ1615.3-3255 and YLW8 have been observed with *VLT/VISIR* and present [Ne II] emission lines blueshifted by several km/s, implying on-going photoevaporation (Pascucci & Sterzik 2009; Sacco et al. 2012). GM Aur has been observed with *Gemini/TEXES*, but with insufficient S/N to precisely determine the line centroid (Najita et al. 2009). While photoevaporation has been detected from these objects, the rate at which gas is lost via this mechanism is still unknown. If [Ne II] is tracing the very thin EUV irradiated region, the mass loss rate is negligible ($\sim 10^{-10} M_{\odot}/yr$); while, if [Ne II] is tracing the deeper X-ray irradiated layer, the mass loss rate may be significant ($\sim 10^{-8} M_{\odot}/yr$). In the latter case, if we assume that full disks start with a mass of $\sim 22\, M_{Jupiter}$ (the mean value derived from millimeter data; see *Section 2.3.3*), they could loose half of their gas mass in just 1 Myr via photoevaporation.

Planet-disk interactions may also provide a mechanism for reducing the gas-to-dust ratio in protoplanetary disks (e.g. Espaillat 2013). Rice et al. (2006) showed that pressure gradients at the outer edge of a gap cleared by a giant planet can act as dust filters. In such a scenario, small dust grains and gas flow across the gap and are either lost to the planet or the inner disk (and eventually the host star), while large dust grains remain trapped in the outer disk. This has the effect of removing gas from the outer disk while retaining most of the mm- and cm-size dust, and thus decreasing the gas-to-dust ratio of the outer disk. However, the leak of small, micron-size dust particles into the inner disk still necessitates some additional mechanism, such as dust coagulation, to explain the dust cavities in transitional disks (Zhu et al. 2012). Additionally, dust filtration alone is not a realistic mechanism for a decreasing the gas-to-dust ratio by 0.5 dex, as suggested by our work. As gas leaves the outer disk and flows into the gap formed by the planet, it will either be accreted onto the planet, or completely cross the gap into the inner disk, where it can then accrete onto the central star. Lubow & D'Angelo (2006) showed that when mass flows across into these gaps formed by giant planets, $\sim 90\%$ of the mass will be accreted onto the planet. Thus, for dust filtration to be the driver of a low gas-to-dust ratio in the outer disk, it is at the expense of putting a large majority of the outer disks's gas mass directly into planets. If we assume full disks start with a gas mass of $\sim 22\, M_{Jupiter}$ (the mean value derived from millimeter data; see *Section 2.3.3*), $\sim 7\, M_{Jupiter}$ of gas would need to be lost to planet formation to result in a decrease in the gas-to-dust of 0.5 dex. If instead, we assume that a full protoplanetary disk can be characterized by a minimum mass solar nebula (MMSN, Weidenschilling 1977; Kuchner 2004), then it would be necessary for the disk to lose even more mass: upwards of $\gtrsim 20\, M_{Jupiter}$[10]. These simple calculations also assume that all of the dust in the outer disk is somehow protected, perhaps

[10]The total disk mass is calculated by integrating the surface mass density from the inner edge of the protoplanetary disk ($\sim$ 0.07 AU) to the outer edge (conservatively, $\sim$ 40 AU). Using the MMSN described by Kuchner (2004) ($\Sigma = 4225\ g/cm^2\ (a/1\ AU)^{-1.78}$) results in a total disk mass of 24 $M_{Jupiter}$. Using the classical MMSN described by Weidenschilling (1977) ($\Sigma = 4200\ g/cm^2\ (a/1\ AU)^{-1.5}$) results in a total disk mass of 38 $M_{Jupiter}$. A loss of 0.5 dex of the disk mass for these two models correspond to 17 and 26 $M_{Jupiter}$, respectively. Using more liberal estimates of the outer edge of the protoplanetary disk (e.g. 270 AU; Chiang & Goldreich 1997) results in even larger masses.

due to a planet-induced pressure bump. If the loss of dust across the gap is large, these mass estimates would only be lower limits. If all of this mass is lost to forming planets, this would suggest the formation of a large number of giant planets at large semimajor axes ($\gtrsim$ 10 AU), which does not seem to agree with the current (though still debated) statistics of giant exoplanets (Nielsen et al. 2013; Fressin et al. 2013; Biller et al. submitted). Lastly, while large, Jovian-mass planets can clear gaps and cause global depletions in the gas surface density of disks, they only deplete the surface density of the disk by a factor of a few (e.g. Fig. 3 of Lubow & D'Angelo 2006). As discussed in Bruderer (2013) (and in *Section 4.4*) our observed factor of 2 line flux difference between transitional disks and full disks would require a drop in the surface density by a factor of $\gtrsim$ 100.

6.2. Potential Followup Observations

Direct measurement of the gas-to-dust ratio in full disks and transitional disks would break our observed degeneracy between gas-to-dust ratio and disk flaring. While the dust mass of protoplanetary disks can be estimated with millimeter observations (e.g. Mohanty et al. 2013), the total gas mass of protoplanetary disks is difficult to directly measure. Combining our observations of the [OI] 63.18 μm line with low J CO rotational lines, has been suggested as a possible way to directly measure total disk gas mass. While this method has been implemented for select, well studied disks (e.g. TW Hya, Thi et al. 2010), its reliability is still under discussion (Gorti & Hollenbach 2009; Bergin et al. 2013). Both low J CO and [OI] lines are optically thick, which make them both primarily sensitive to temperature - and only weakly dependent on disk mass. Alternatively, observations of isotopologues may provide direct estimates for disk mass. Isotopologues (such as ^{13}C) are minor components within the disk and can be optically thin and directly trace disk mass (modulo the assumed abundances of the relative species). With the significant ($\sim$ 10x) increase in sensitivity allowed by ALMA, detecting emission from minor disk components out to nearby star-forming regions (e.g. Taurus-Auriga) is now possible.

It is difficult to directly measure the flaring of *gas* in protoplanetary disks. For select nearby and edge-on disks, it may be possible to directly measure the relative vertical distribution of dust (via mm-emission) and gas (via gas emission lines, such as CO and its isotopologues) with high spatial and spectral resolution observations with ALMA (Rosenfeld et al. 2013). Detailed SED modeling covering the mid-infrared, far-infrared, and millimeter wavelengths may be able to break the degeneracy between disk gas mass and disk scale height. Flared disks intercept more stellar radiation at larger semimajor axes than flatter disks. Emission from these warm, outer disk, surface layers dominate the SED beyond $\sim$20 μm (Chiang & Goldreich 1997).

7. Summary

We obtained *Herschel*/PACS spectra of [OI] 63.18 μm for 21 transitional disks in the Ophiuchus, Chameleon, and Lupus star forming regions. This survey complements the larger *Herschel* GASPS survey of the Taurus star forming region (Dent et al. 2013) by quadrupling the number of transitional disks observed with PACS in this wavelength. [OI] 63.18 μm is significant because it traces the cool, outer regions ($\gtrsim$ 10 AU) of the protoplanetary disk, where the majority of the disk mass lies. Our primary results can be summarized as follows:

1. Full disks have larger [OI] 63.18 μm line luminosities than transitional disks, while having similar 63.18 μm continuum luminosities. While this result was previously recognized by Howard et al. (2013) for the GASPS Taurus-Auriga sample, our data extends this trend to a larger sample of transitional disks, suggesting that lower [OI] 63.18 μm line emission is a characteristic property of transitional disks.

2. For all of our targets, we self-consistently derived stellar and disk parameters that have been previously shown to affect [OI] 63.18 μm emission. While [OI] 63.18 μm can correlate with these parameters, we found that transitional disks and full disks have statistically indistinguishable effective tempera-

tures, bolometric luminosities, FUV luminosities, accretion rates, and X-ray luminosities. Thus, these properties cannot be responsible for the lower [OI] 63.18 μm line luminosities of transitional disks.

3. We found no correlation between the [OI] 63.18 μm line luminosities of transitional disks and either their disk masses (as inferred from millimeter photometry), dust cavity sizes, or wall heights (as inferred from SED and interferometric image modeling). This suggests that the decrease in [OI] 63.18 μm emission is not simply due to a lack of material in the inner cavity of transitional disks, though more modeling is needed to confirm this result (e.g. Bruderer 2013).

4. Using the DENT grid of thermo-chemical protoplanetary disk models (Woitke et al. 2010), we determined that the lower [OI] 63.18 μm line luminosities in transitional disks could result from either a decrease in disk flaring, or a decrease in gas-to-dust ratio via a global depletion of gas mass. Decreasing the disk flaring results in less stellar irradiation impinging on the surface of the outer disk, thus decreasing the disk temperature and reducing [OI] 63.18 μm emission. Decreasing the gas-to-dust ratio by removing gas mass results in a decrease in the amount of heating from H_2 photo-dissociation, collisional de-excitation of H_2^*, and/or photo-electric heating (e.g. Woitke et al. 2009). Both photoevaporation, and planet formation, can result in a decrease in gas mass, although their efficiencies are still not well constrained. While additional observations are needed to disentangle the effects of disk flaring and gas-to-dust ratio, our results show that transitional disks are more evolved than their full disk counterparts, possibly even at large radii.

I. P., J. T. K., C. E., and S. A. acknowledge NASA/JPL for funding support. J. T. K. and I. P. thank Elisabetta Rigliaco for helpful discussions on mass accretion rate estimates. The authors would also like to thank the referee, Kees Dullemond, for a very constructive review.

A. Supplementary Figures

Figure 7 includes all of the reduced *Herschel*/PACS [OI] 63.18 μm spectra used in this work, and are only provided in the online version of the article. *Figures 8* through *16* display null correlations of various stellar and disk parameters with the [OI] 63.18 μm line luminosity and nearby continuum luminosity and are only provided in the online version of the article.

REFERENCES

Aikawa, Y., Nomura, H. 2006, ApJ, 642, 1152.

Alcalá, J. M., Covino, E., Sterzik, M. F. et al. 2000, A&A, 355 629

Alexander, R. D., Clarke, C. J., Pringle, J. E. 2006, MNRAS, 369, 229

Alexander, R. D., Pascucci, I., Andrews, S., Armitage, P., Cieza, L. 2014, in Protostars and Planets VI, ed. H. Beuther, C. Dullemond, T. Henning, R. Klessen, in prep. (arXiv:1311.1819)

Andrews, S. M., Wilner, D. J., Hughes, A. M., Qi, C., Dullemond, C. P. 2009, ApJ, 700, 1502

Andrews, S. M., Williams, J. P. 2005, ApJ, 631, 1134

Andrews, S. M., Rosenfeld, K. A., Wilner, D. J., Bremer, M. 2011, ApJ, 732, 42

Antoniucci, S., Garcí López, R., Nisini, B. et al. 2011, A&A, 534, 32.

Aresu, G., Kamp, I., Meijerink, R., Woitke, P. et al. M. 2011, A&A, 526, 163

Aresu, G., Meijerink, R., Kamp, I. et al. 2012, A&A, 547, 69

Aresu, G., Kamp, I., Meijerink, R. et al. (2014), A&A, accepted

Bary, J. S., Weintraub, D. A., Shukla, S. J., Leisenring, J. M., Kastner, J. H. 2008, ApJ, 678, 1088

Biller, B. A., Liu, M. C., Wahhaj, Z. et al. 2013, ApJ, 777, 160

Biazzo, K., Alcalá, J. M., Covino, E. et al. L. 2012, A&A, 547, 104

Beckwith, S. V. W., Sargent, A. I., Chini, R. S., Guesten, R. 1990, AJ, 99, 924

Bergin, E. A., Cleeves, L. I., Gorti, U. et al. 2013, Nature, 493, 644

Bouvier, J., Appenzeller, I. 1992, A&AS, 92 481

Bouvier, J., Cabrit, S., Fernandez, M., Martin, E. L., Matthews, J. M. 1993, A&AS, 101, 485

Brandner, W., Alcala, J. M., Kunkel, M., Moneti, A., Zinnecker, H. 1996, A&A, 307, 121

Briceño, C., Calvet, N., Kenyon, S., Hartmann, L. 1999, AJ, 118, 1354

Brown, J. M., Blake, G. A., Dullemond, C. P. et al. 2007, ApJ, 664, 107

Brown, J. M., Blake, G. A., Qi, C., Dullemond, C. P. et al. 2009, ApJ, 704, 496

Bruderer, S. 2013, A&A, 559, A46.

Cabrit, S., Edwards, S., Strom, S. E., Strom, K. M. 1990, ApJ, 354, 687

Calvet, N., D'Alessio, P., Hartmann, L. et al. 2002, ApJ, 658, 1008

Carkner, L., Kozak, J. A., Feigelson, E. D. 1998, AJ, 116, 1933

Chen, H., Myers, P. C., Ladd, E. F., Wood, D. O. S. 1995, ApJ, 445, 377

Chiang, E. I., Goldreich, P. 1997, ApJ, 490, 368

Cohen, M., Kuhi, L. V. 1979, ApJS, 41, 743

Cutri, R. M., Skrutskie, M. F., van Dyk, S. et al. 2003, yCat, 2246, 0

D'Alessio P. D., Calvet, N., Hartmann, L., Franco-Hernández, R., Servín, H. 2006, ApJ, 638, 314

Daemgen, S., Petr-Gotzens, M., Correia, S. et al. 2013, A&A, 554, 43

Dahm, S. E. 2008, AJ, 136, 521

Damiani, F., Micela, G., Sciortino, S., Harnden, F. R. Jr. 1995, ApJ, 446, 331

DENIS Consortium 2005, VizieR Online Data Catalog, 2263, 0

Dent, W. R. F., Thi, W. F., Kamp, I. et al. 2013, PASP, 125, 477

Dullemond, C. P., Dominik, C. 2005, A&A, 434, 971

Dutrey, A., Guilloteau, S., Simon, M. 2003, A&A, 402, 1003

Edwards, S., Cabrit, S., Strom, S. E. et al. 1987, ApJ 321, 473

Edwards, S., Hartigan, P., Ghandour, L., Andrulis, C., 1994, AJ, 108, 1056

Espaillat, C., Calvet, N., D'Alessio, P. et al. 2007, ApJ, 670, L135

Espaillat, C., D'Alessio, P., Hernández, J., et al. 2010, ApJ, 717, 441

Espaillat, C., Furlan, E., D'Alessio, P. et al. 2011, ApJ, 728, 49

Espaillat, C., Ingleby, L., Hernández, J. et al. 2012, ApJ, 747, 103

Espaillat, C. 2013, International Astronomical Union Symposium 299

Espaillat, C. et al. 2014, in Protostars and Planets VI, ed. H. Beuther, C. Dullemond, T. Henning, R. Klessen, in prep.

Fang, M., van Boekel, R., Wang, W. et al. 2009, A&A, 504, 461

Feigelson, E. D., Kriss, G. A. 1989, ApJ, 338, 262

Feigelson, E. D., Casanova, S., Montmerle, T., Guibert, J. 1993, ApJ, 416, 623

Fernandez, M. 1995, A&AS, 113, 473

Fressin, F., Torres, G., Charbonneau, D. et al. 2013, ApJ, 766, 81

Furlan, E., Watson, D. M., McClure, M. K. et al. 2009, ApJ, 703, 1964

Gauvin, L. S., Strom, K. M. 1992, ApJ, 385, 217

Gorti, U., Hollenbach, D. 2008, ApJ, 683, 287

Gorti, U., Hollenbach, D. 2009, ApJ, 690, 1539

Gorti, U., Hollenbach, D., Najita, J., Pascucci, I. 2011, ApJ, 735, 90

Güdel, M., Briggs, K. R., Arzner, K. et al. 2007, A&A, 468, 353

Guenther, E. W., Emerson, J. P. 1997, A&A, 321, 803

Guenther, E. W., Esposito, M., Mundt, R. 2007, A&A, 467, 1147

Guilloteau, S., Dutrey, A., Piétu, V., Boehler, Y. 2011, A&A, 529, 105

Gullbring, E., Hartmann, L., Briceno, C., Calvet, N. 1998, ApJ, 492, 323

Hartigan, P., Edwards, S., Ghandour, L. 1995, ApJ, 452, 736

Hartmann, L., Calvet, N., Gullbring, E., D'Alessio, P. 1998, ApJ, 495, 385

Henning, T., Pfau, W., Zinnecker, H., Prusti, T. 1993, A&A, 276, 129

Herbst, W., Herbst, D. K., Grossman, E. J., Weinstein, D. 1994, AJ, 108, 1906

Herczeg, G. J., Najita, J. R., Hillenbrand, L. A., Pascucci, I. 2007, ApJ, 670, 509

Herczeg, G. J., Hillenbrand, L. A. 2008, ApJ, 681, 594

Howard, C. D., Sandell, G., Vacca, W. D. et al. 2013, ApJ, 776, 21

Hughes, J., Hartigan, P., Krautter, J., Kelemen, J. 1994, AJ, 108, 1071

Hughes, A. M., Wilner, D. J., Andrews, S. M. Qi, C., Hogerheijde, M. R. 2011, ApJ, 727, 85

Ireland, M. J., Kraus, A. L. 2008, ApJ, 678, 59

Kastner, J. H., Huenemoerder, D. P., Schulz, N. S., Weintraub, D. A. 1999, ApJ, 525, 837

Kamp, I., Tilling, I., Woitke, P., Thi, W.-F., Hogerheijde, M. 2010, A&A, 510, 18

Kamp, I., Woitke, P., Pinte, C. et al. 2011, A&A, 532, 85

Kelly, B. C. 2007, ApJ, 665, 1489

Kenyon, S. J., Hartmann, L. 1995, ApJS, 101, 117

Kenyon, S. J., Brown, D. I., Tout, C. A., Berlind, P. 1998, AJ, 115, 2491

Kenyon, S. J., Gomez, M., Whitney, B. A. 2008, in Handbook of Star Forming Regions, Volume 1, ed. B. Reipurth (San Francisco, CA: ASP), 405

Kim, K. H., Watson, D. M., Manoj, P. et al. 2009, ApJ, 700, 1017

Kim, K. H., Watson, D. M., Manoj, P. et al. 2013, ApJ, 769, 149

Kraus, A. L., Hillenbrand, L. A. 2009, ApJ, 704, 531

Kraus, A. L., Ireland, M. J., Hillenbrand, L. A., Martinache, F. 2012, ApJ, 745, 19

Kuchner, M. J. 2004, ApJ, 612, 1147

LaValley M., Isobe, T., Feigelson, E. 1992, ASPC, 25, L245

Lubow, S. H., Seibert, M., Artymowicz, P. 1999, ApJ, 526, 1001

Lubow, S. H., D'Angelo, G. 2006, ApJ, 641, L526

Luhman, K. L. 1999, ApJ, 525, 466

Luhman, K. L. 2000, ApJ, 544, 1044

Luhman, K. L. 2004, ApJ, 602, 816

Luhman, K. L. 2007, ApJS, 173, 104

Magazzu, A., Rebolo, R., Pavlenko, I. V. 1992, ApJ, 392, 159

Mathis, J. S. 1990, ARA&A, 28, 37

McCabe, C., Ghez, A. M., Prato, L. 2006, ApJ, 636, 932

McClure, M. K., Furlan, E., Manoj, P. et al. 2010, ApJS, 188, 75

Meeus, G., Pinte, C., Woitke, P. et al. 2010, A&A, 518, L124

Meeus, G., Montesinos, B., Mendigutía, I. et al. 2012, A&A, 544, 78

Meijerink, R., Aresu, G., Kamp, I. et al. 2012, A&A, 547, 68.

Merín, B., Jørgensen, J., Spezzi, L. et al. 2008, ApJS, 177, 551

Merín, B., Brown, J. M., Oliveira, I. et al. 2010, ApJ, 718, 1200

Mohanty, S., Greaves, J., Mortlock, D. et al. 2013, ApJ, 773, 168

Monet, D. G., Levine, S. E., Canzian, B. et al. 2003, AJ, 125, 984

Muzerolle, J., Calvet, N., Hartmann, L. 1998, ApJ, 492, 743

Muzerolle, J., Hillenbrand, L., Calvet, N., Briceño, C. Hartmann, L. 2003, ApJ, 592, 266

Muzerolle, J., Allen, L. E. et al. 2010, ApJ, 708, 1107

Najita, J. R., Strom, S. E., Muzerolle, J. 2007, MNRAS, 378, 369

Najita, J. R., Doppmann, G. W., Bitner, M. A. et al. 2009, ApJ, 697, 957

Neuhaeuser, R., Sterzik, M. F., Schmitt, J. H. M. M., Wichmann, R., Krautter, J. 1995, A&A, 297, 391

Nielsen, E. L., Liu, M. C., Wahhaj, Z. et al. 2013, ApJ, 776, 4

Nuernberger, D., Chini, R., Zinnecker, H., 1997, A&A, 324, 1036

Osterloh, M., Beckwith, S. V. W. 1995, ApJ, 539, 288

Ott, S. 2010, ASPC, 434, 139

Pascucci, I., Apai, D., Hardegree-Ullman, E. E. et al. 2008, ApJ, 673, 477

Pascucci, I., Sterzik, M. 2009, ApJ, 702, 724

Pascucci, I., Tachibana, S. 2010, in Protoplanetary Dust: Astrophysical and Cosmochemical Perspectives, eds. D. Apai & D. S. Lauretta (Cambridge: Cambridge University Press), 263

Pinte, C., Woitke, P., Ménard, F. et al. 2010, A&A, 518, L126

Podio, L., Kamp, I., Flower, D. et al. 2012, A&A, 545, 44

Poglitsch, A., Waelkens, C., Geis, N. et al. 2010, A&A, 518, L2

Prato, L., Greene, T. P., Simon, M. 2003, ApJ, 584, 853

Rebull, L. M., Padgett, D. L., McCabe, C.-E. 2010, ApJS, 186, 259

Riaz, B., Gizis, J. E., Hmiel, A. 2006, ApJ, 639, 79

Rigliaco, E., Natta, A., Randich, S. et al. 2011, A&A, 526, L6

Rigliaco, E., Natta, A., Testi, L. et al. 2012, A&A, 548, 56

Rice, W. K. M., Armitage, P. J., Wood, K., Lodato, G. 2006 MNRAS, 372, L9

Riviere-Marichalar, P., Ménard, F., Thi, W. F. et al. 2012 A&A, 538, L3

Rosenfeld, K. A., Andrews, S. M., Wilner, D. J., Kastner, J. H., McClure, M. K. 2013, ApJ, 775, 136

Sacco, G. G., Flaccomio, E., Pascucci, I. et al. 2012, ApJ, 747, 142

Salyk, C., Blake, G. A., Boogert, A. C. A., Brown, J. M. 2009, ApJ, 699, 330

Schisano, E., Covino, E., Alcalá, J. M. et al. 2009, A&A, 501, 1013

Shu, F., Najita, J., Ostriker, E. et al. 1994, ApJ, 429, 781

Siess, L., Dufour, E., Forestini, M. 2000, A&A, 358, 593

Spezzi, L., Alcalá, J. M, Frasca, A., Covino, E., Gandolfi, D. 2007, A&A, 470, 281

Strom, K. M., Strom, S. E., Edwards, S., Cabrit, S. Skrutskie, M. F. 1989, AJ, 97, 1451

Taguchi, Y., Itoh, Y., Mukai, T. 2009, PASJ, 61, 251

Thi, W.-F., Mathews, G., Ménard, F. et al. 2010, A&A, 518, L125

Weidenschilling, S. J. 1977, Ap&SS, 51, 153

White, N. E., Giommi, P., Angelini, L. 2000, yCat, 9031, 0

White, R. J., Ghez, A. M. 2001, ApJ, 556, 265

White, R. J., Basri, G. 2003, ApJ, 582, 1109

Williams J. P., Cieza, L. A. 2011, ARA&A, 49, 67

Wilking, B. A., Meyer, M. R., Robinson, J. G., Greene, T. P. 2005, AJ, 130, 1733

Woitke, P., Pinte, C., Tilling, I. et al. 2010, A&A, 510, 18

Woitke, P., Kamp, I., Thi, W.-F. 2009, A&A, 501, 383

Yang, H., Herczeg, G. J., Linsky, J. L. et al. 2012, ApJ, 744, 121

Zhu, Z., Nelson, R. P., Dong, R., Espaillat, C. Hartmann, L. 2012, ApJ, 755, 6

This 2-column preprint was prepared with the AAS LaTeX macros v5.2.

,

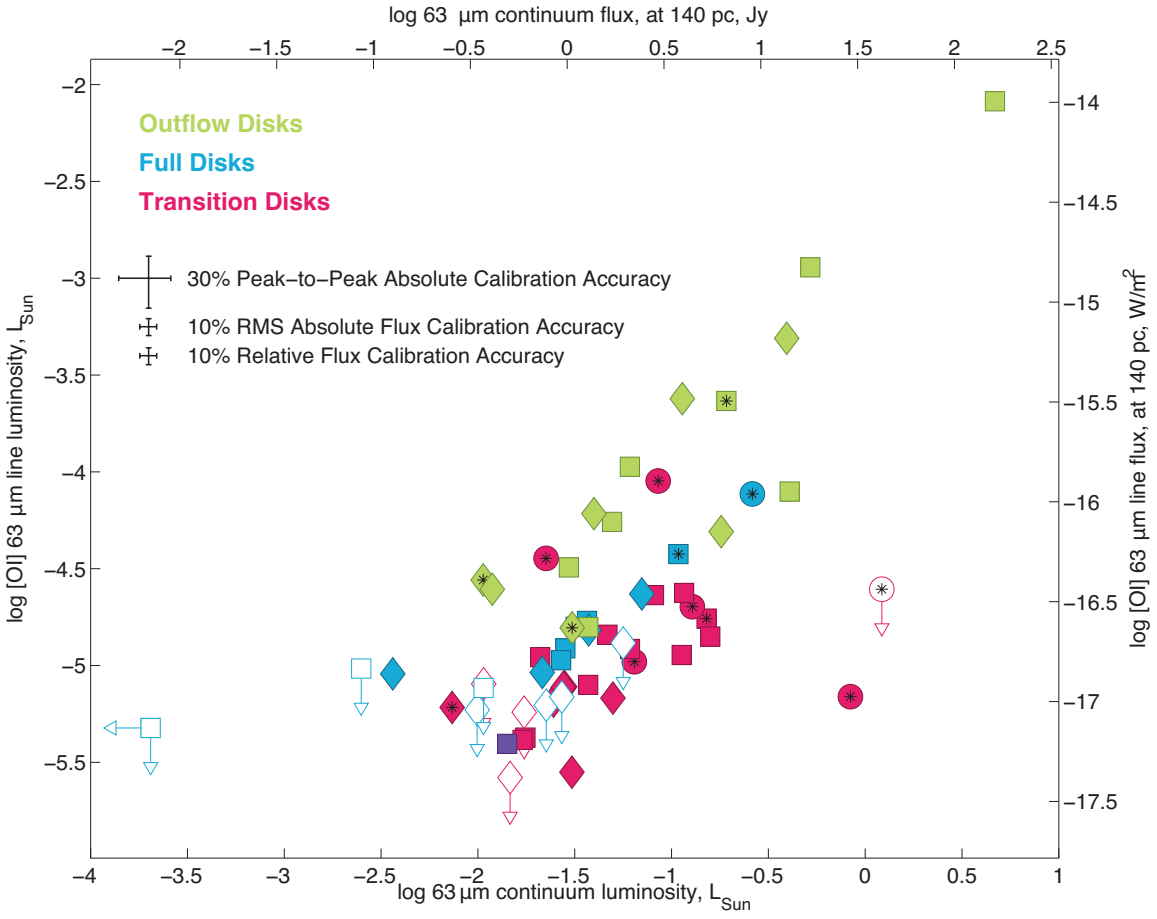
log 63 µm continuum flux, at 140 pc, Jy
log [OI] 63 µm line luminosity, L_Sun
log [OI] 63 µm line flux, at 140 pc, W/m^2
log 63 µm continuum luminosity, L_Sun
Outflow Disks
Full Disks
Transition Disks
30% Peak–to–Peak Absolute Calibration Accuracy
10% RMS Absolute Flux Calibration Accuracy
10% Relative Flux Calibration Accuracy

Fig. 1a.— [OI] 63.18 μm line luminosity as a function of 63 μm continuum luminosity for our sample of transitional disks (red), full disks (blue), and outflow disks (green). 3σ upper limits are denoted by hollow data points with arrows. Symbols correspond to stellar spectral types: circles are G-type stars (which are included in this plot, but neglected in the statistical analysis, for reasons described in the paper), squares are K-type stars, and diamonds are M-type stars. BP Tau (an evolved full disk) is indicated in purple. Targets excluded from statistical tests (for either being a binary that does not meet the criteria in Sect. 2.1, or being a G-type star) are marked by an asterisks.

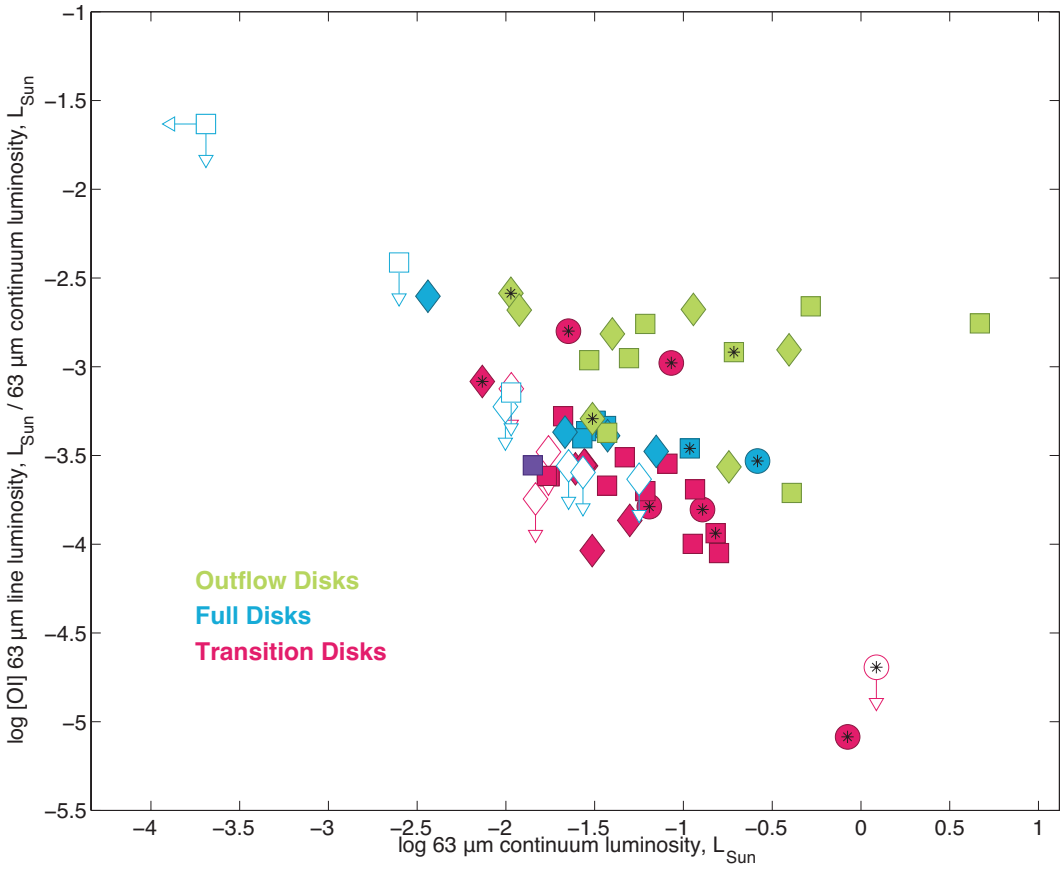

Fig. 1b.— The ratio of [OI] 63.18 μm line luminosity / 63 μm continuum luminosity as a function of 63 μm continuum luminosity for our sample of transitional disks (red), full disks (blue), and outflow disks (green). 3σ upper limits are denoted by hollow data points with arrows. Symbols are as in *Figure 1a*.

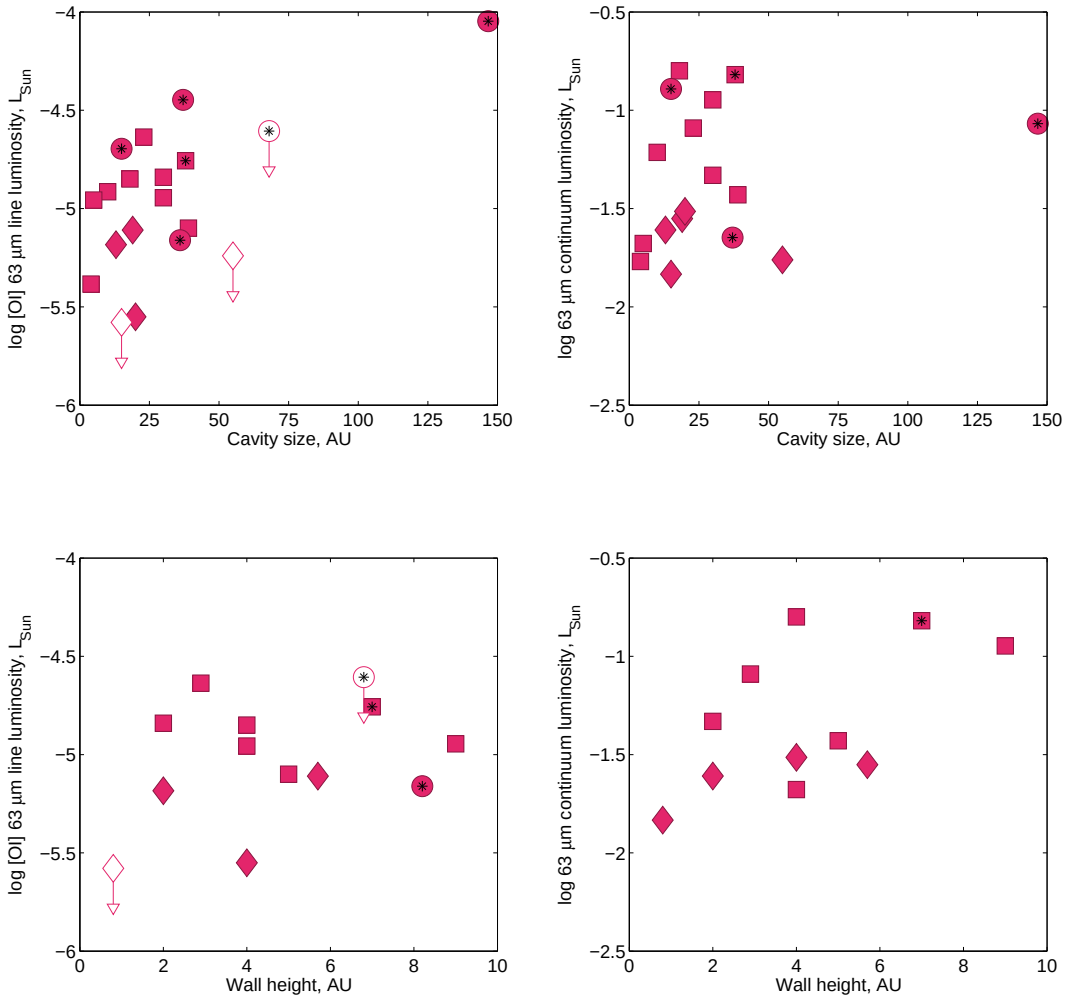
log [OI] 63 µm line luminosity, L_Sun
Cavity size, AU
log 63 µm continuum luminosity, L_Sun
Cavity size, AU
log [OI] 63 µm line luminosity, L_Sun
Wall height, AU
log 63 µm continuum luminosity, L_Sun
Wall height, AU

Fig. 2.— [OI] 63.18 μm line luminosity and 63 μm continuum luminosity as a function of gap size and wall height for all of the transitional disks within our sample for which such measurements have been made in the past. 3σ upper limits are denoted by hollow data points with arrows. Symbols are as in *Figure 1a*.

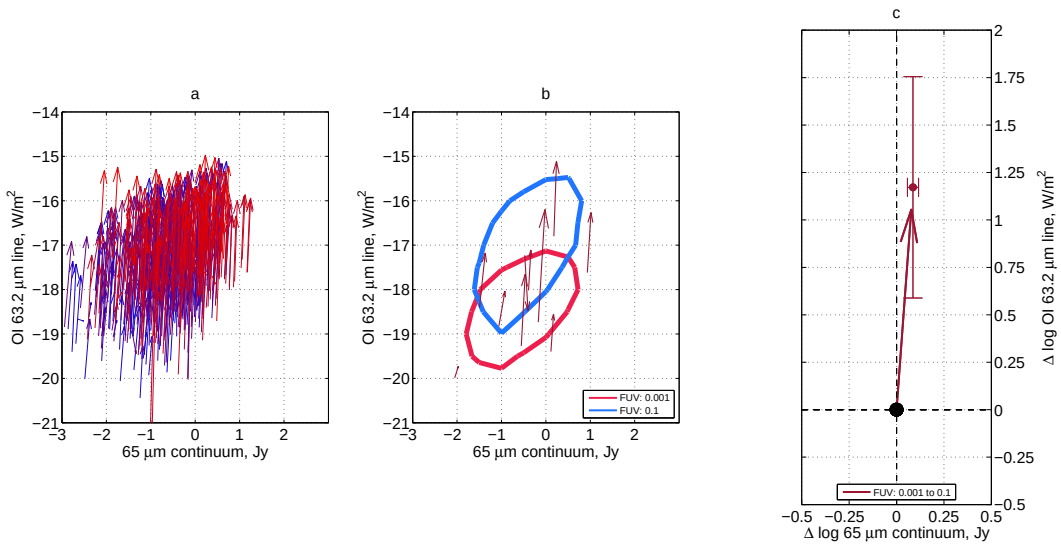

Fig. 3.— DENT grid predictions for how [OI] 63.18 μm line flux and 65 μm continuum flux change, with increasing disk FUV excess (FUV = 0.001 and 0.1), for a random subsample (N $\sim$ 5000) of disks around low mass stars ($\leq$ 1 M_{Sun}). The left shows all of the "evolutionary tracks" for this sample of disk models. The middle panel shows the regions that contain 67% of the models as a function of FUV. The "evolutionary tracks" of 10 randomly selected disk models are included for reference. These tracks indicate the path that that particular disk would move if the FUV increased. The panel on right shows the mean change ("delta") in [OI] 63.18 μm line flux and 65 μm continuum flux, with respect to an initially low FUV disk. Arrows point in the direction of increasing FUV. Error bars indicate the 1σ variations in these Δ [OI] 63.18 μm line flux and Δ 65 μm continuum flux during each step in increasing FUV.

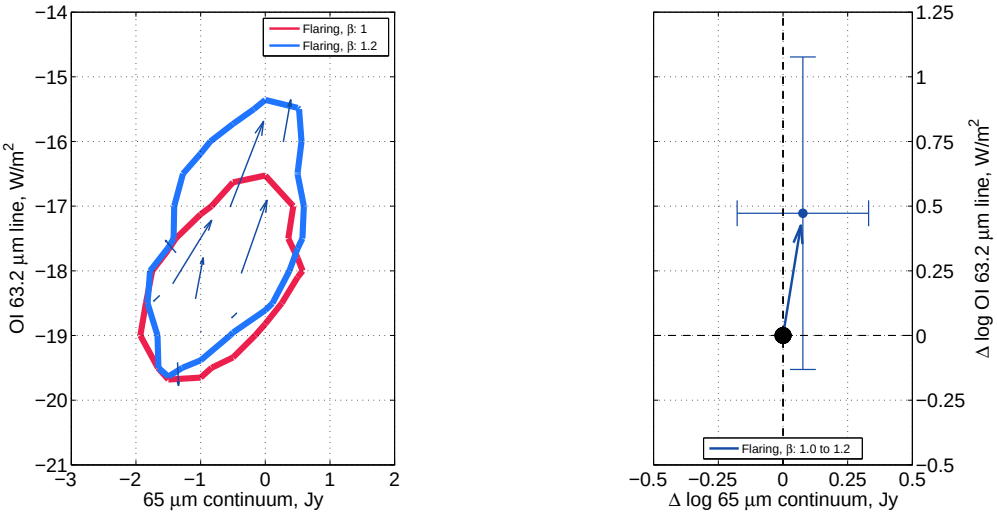

Fig. 4.— DENT grid predictions for how [OI] 63.18 μm line flux and 65 μm continuum flux change, with increasing disk flaring ($\beta = 1.0$ and $\beta = 1.2$), for a random subsample (N $\sim$ 5000) of disks around low mass stars ($\leq$ 1 M_{Sun}). The left panel shows the regions that contain 67% of the models as a function of disk flaring. The "evolutionary tracks" of 10 randomly selected disk models are included for reference. These tracks indicate the path that that particular disk would move if the disk became more flared. The panel on right shows the mean change ("delta") in [OI] 63.18 μm line flux and 65 μm continuum flux, with respect to an initially flatter ($\beta = 1.0$) disk. Arrows point in the direction of increasing disk flaring. Error bars indicate the 1σ variations in these Δ [OI] 63.18 μm line flux and Δ 65 μm continuum flux during each step in increasing flaring.

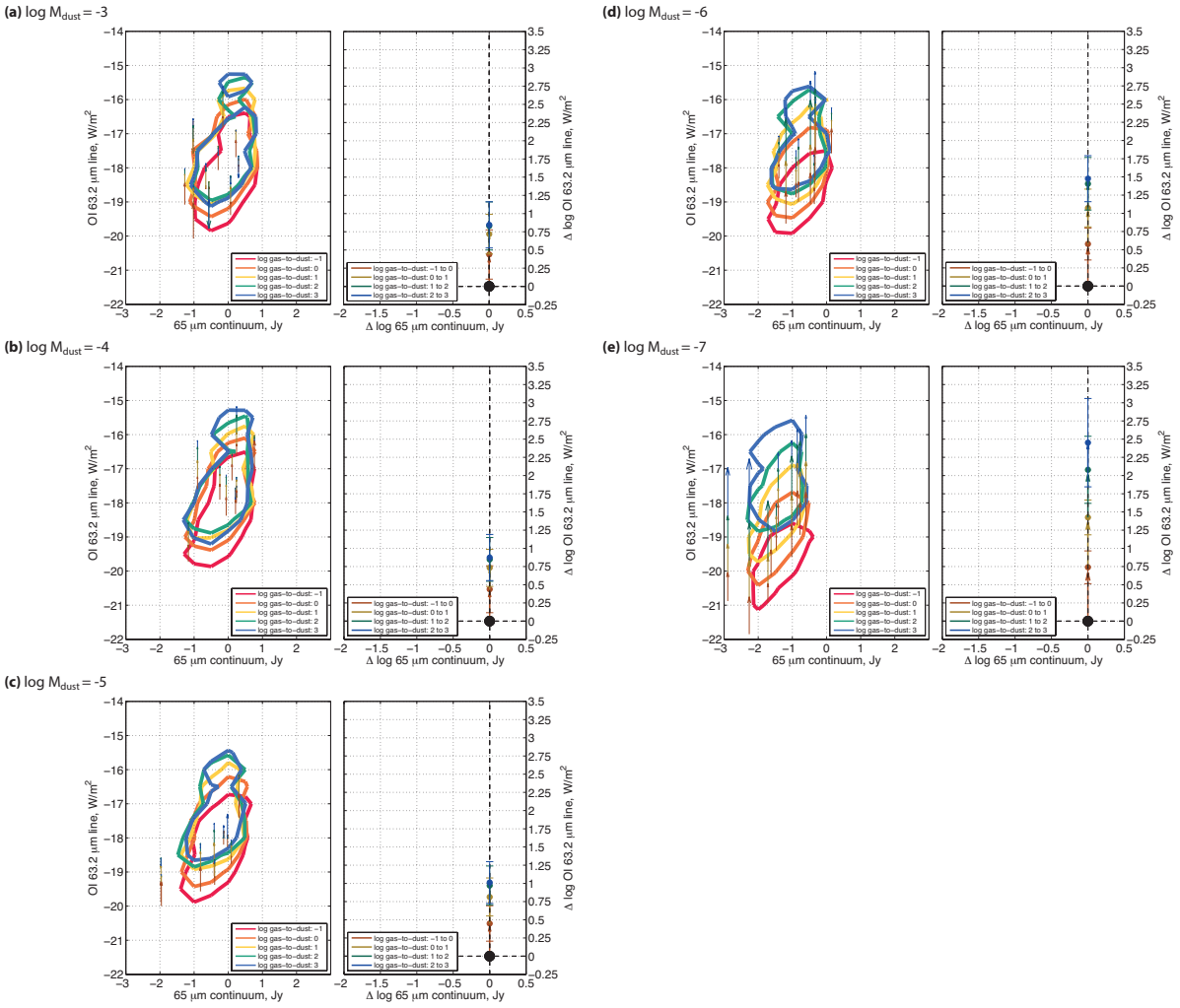
(a) log M_dust = -3
(b) log M_dust = -4
(c) log M_dust = -5
(d) log M_dust = -6
(e) log M_dust = -7
OI 63.2 μm line, W/m²
65 μm continuum, Jy
Δ log 65 μm continuum, Jy
Δ log OI 63.2 μm line, W/m²
log gas−to−dust: −1
log gas−to−dust: 0
log gas−to−dust: 1
log gas−to−dust: 2
log gas−to−dust: 3
log gas−to−dust: −1 to 0
log gas−to−dust: 0 to 1
log gas−to−dust: 1 to 2
log gas−to−dust: 2 to 3

Fig. 5.— DENT grid predictions for how [OI] 63.18 μm line flux and 65 μm continuum flux change, with increasing gas-to-dust ratio, while the dust mass remains fixed. *Figures 5a - 5e* display the effect for different dust masses. Disk models are sampled at random (N $\sim$ 5000), and consist of only low mass stars ($\leq$ 1 M_{Sun}). The panels on the left show the regions that contain 67% of the models as a function of gas-to-dust ratio. The "evolutionary tracks" of 10 randomly selected disk models are included for reference. These tracks indicate the path that that particular disk would move if the gas-to-dust ratio increased. The panels on right show the mean change ("delta") in [OI] 63.18 μm line flux and 65 μm continuum flux, with respect to an initially low gas-to-dust disk. Arrows point in the direction of increasing gas-to-dust ratio (corresponding to increasing gas in these figures). Error bars indicate the 1σ variations in these Δ [OI] 63.18 μm line flux and Δ 65 μm continuum flux during each step in increasing gas-to-dust ratio.

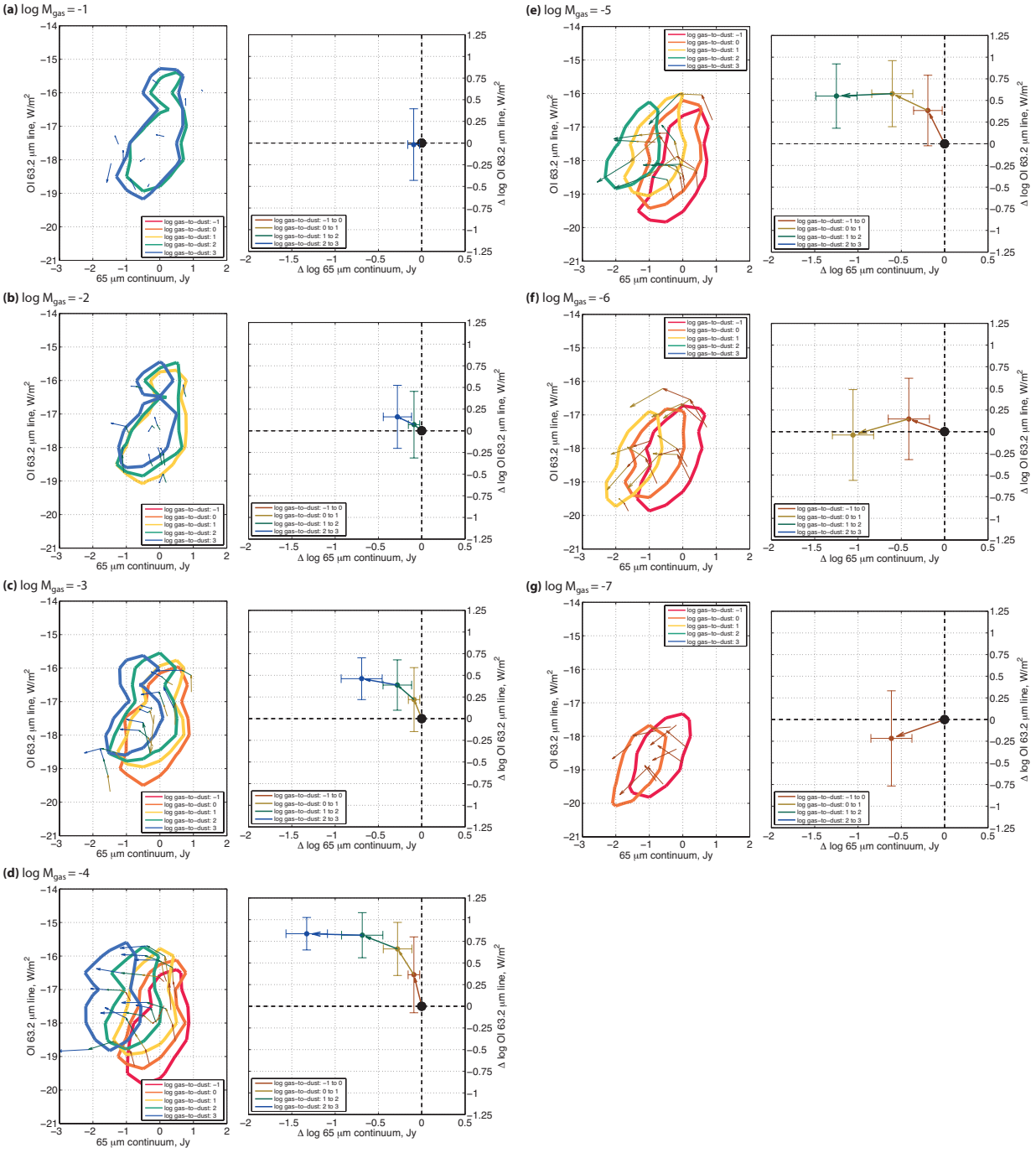
(a) log M_gas = -1
(b) log M_gas = -2
(c) log M_gas = -3
(d) log M_gas = -4
(e) log M_gas = -5
(f) log M_gas = -6
(g) log M_gas = -7
OI 63.2 μm line, W/m²
65 μm continuum, Jy
Δ log 65 μm continuum, Jy
Δ log OI 63.2 μm line, W/m²
log gas−to−dust: −1
log gas−to−dust: 0
log gas−to−dust: 1
log gas−to−dust: 2
log gas−to−dust: 3
log gas−to−dust: −1 to 0
log gas−to−dust: 0 to 1
log gas−to−dust: 1 to 2
log gas−to−dust: 2 to 3

Fig. 6.— DENT grid predictions for how [OI] 63.18 μm line flux and 65 μm continuum flux change, with increasing gas-to-dust ratio, while the gas mass remains fixed. *Figures 6a - 6g* display the effect for different gas masses. Disk models are sampled at random (N $\sim$ 5000), and consist of only low mass stars ($\leq$ 1 M_{Sun}). The panels on the left show the regions that contain 67% of the models as a function of gas-to-dust ratio. The "evolutionary tracks" of 10 randomly selected disk models are included for reference. These tracks indicate the path that that particular disk would move if the gas-to-dust ratio increased. The panels on the right show the mean change ("delta") in [OI] 63.18 μm line flux and 65 μm continuum flux, with respect to an initially low gas-to-dust disk. Arrows point in the direction of increasing gas-to-dust ratio (corresponding to decreasing dust in these figures). Error bars indicate the 1σ variations in these Δ [OI] 63.18 μm line flux and Δ 65 μm continuum flux during each step in increasing gas-to-dust ratio.

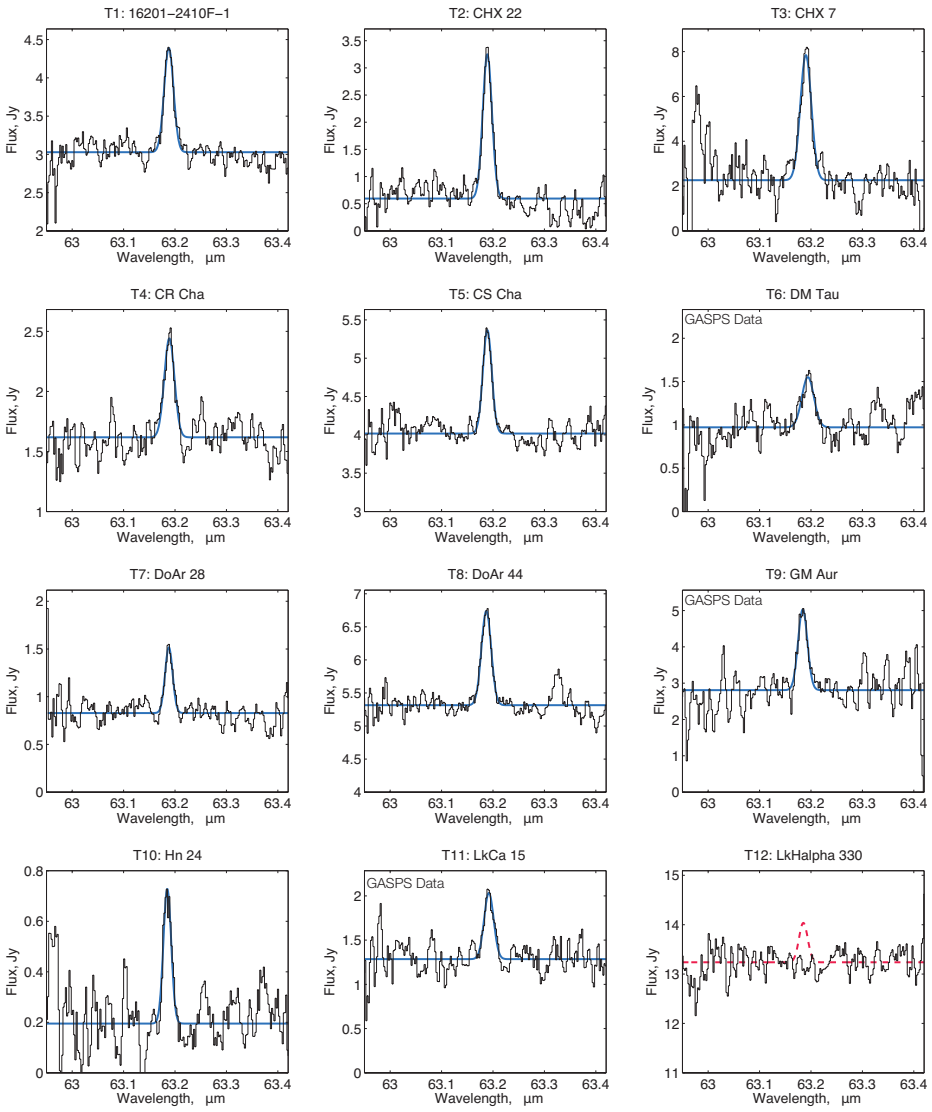

Fig. 7.— ONLINE ONLY. *Herschel*/PACS 63μm spectra. Blue solid lines indicate the best fit Gaussian line profile for the [OI] 63.18 μm line (as discussed in *Section 3*). Red dashed lines depict the hypothetical 3-sigma upper limits. Observations taken by the GASPS team are indicated by the annotation "GASPS Data." While we re-reduced this data, these observations were previously reported in Howard et al. (2013), Meeus et al. (2012), and Podio et al. (2012)

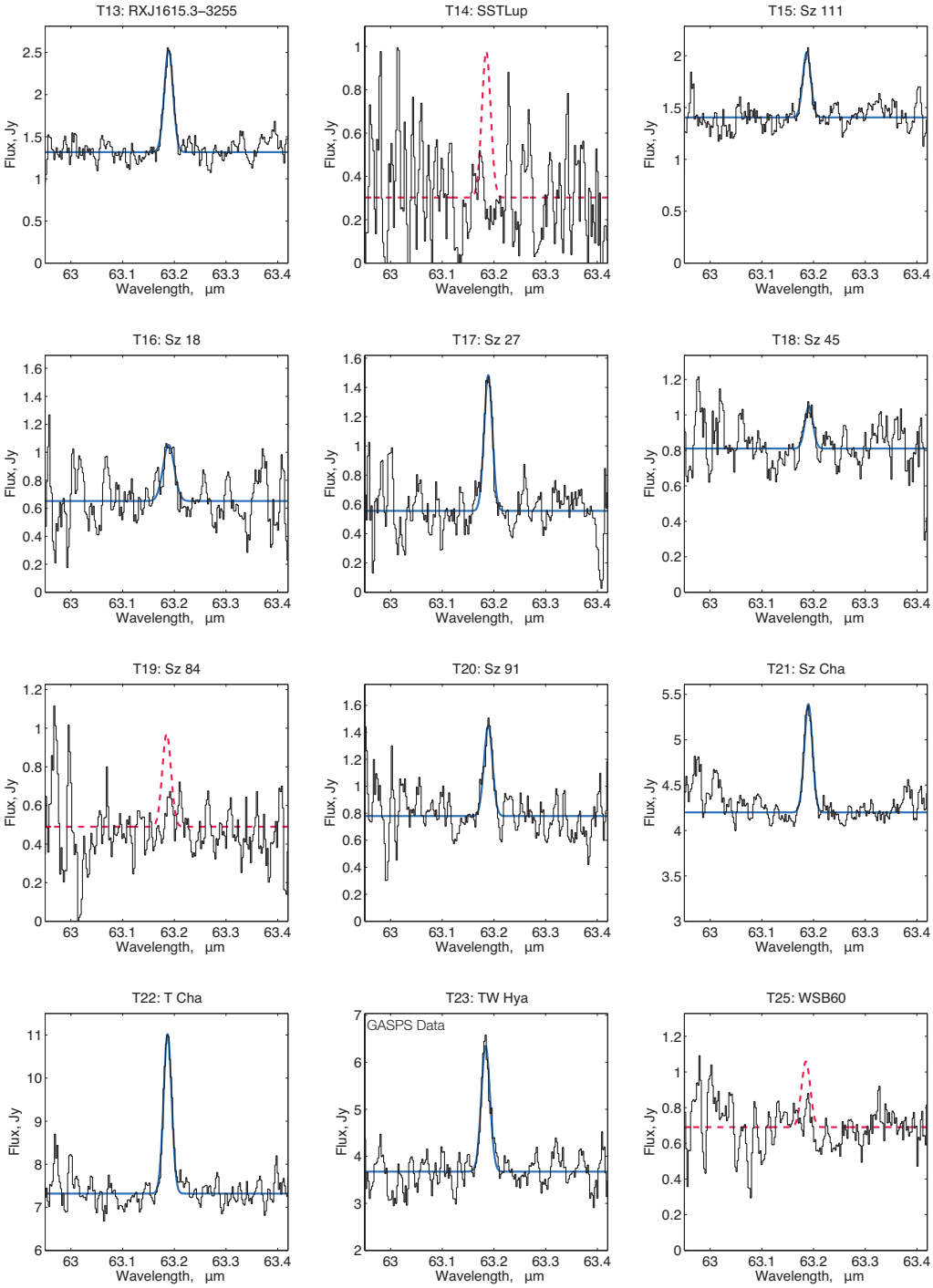

Fig. 7.— continued.

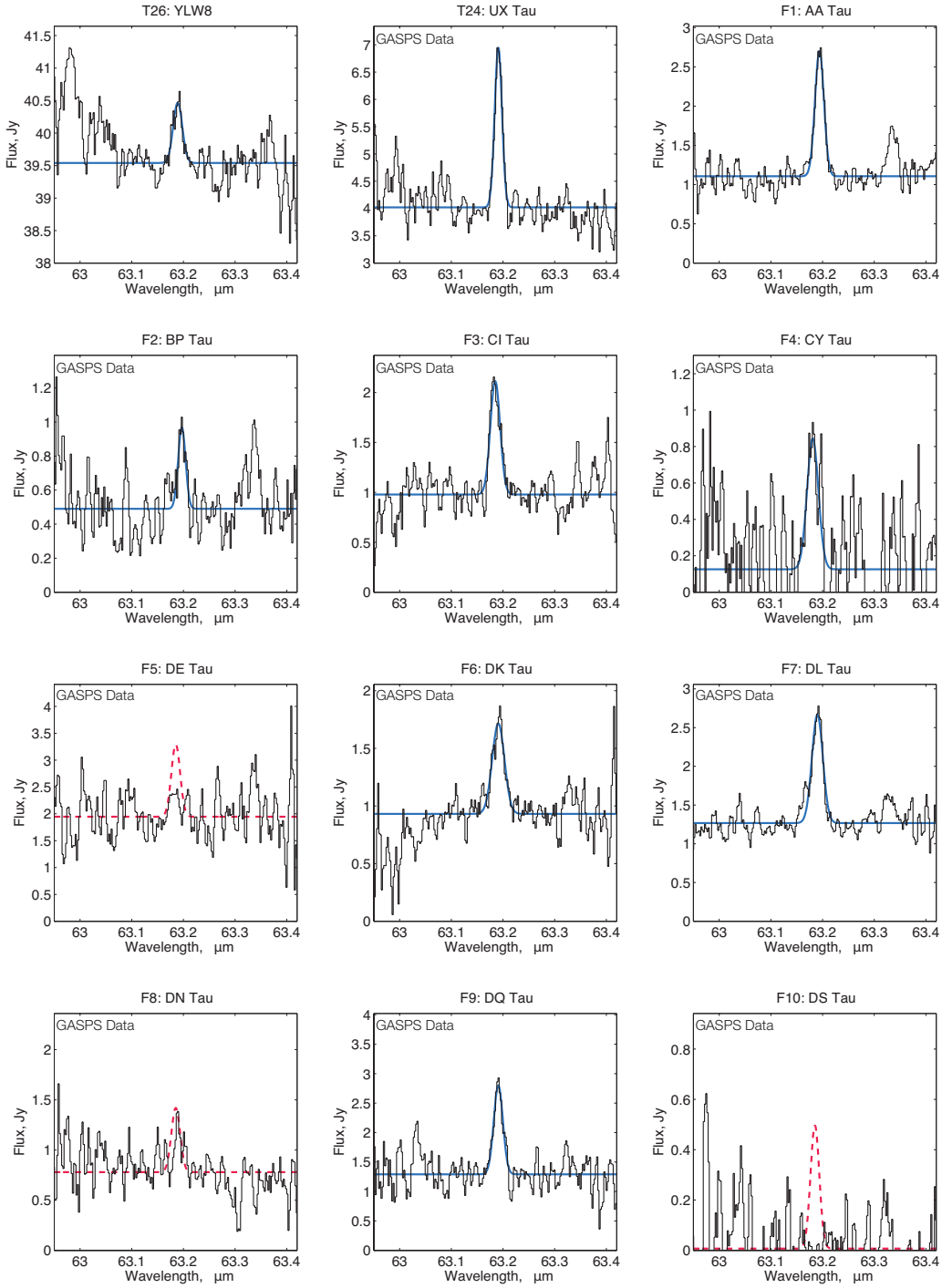

Fig. 7.— continued.

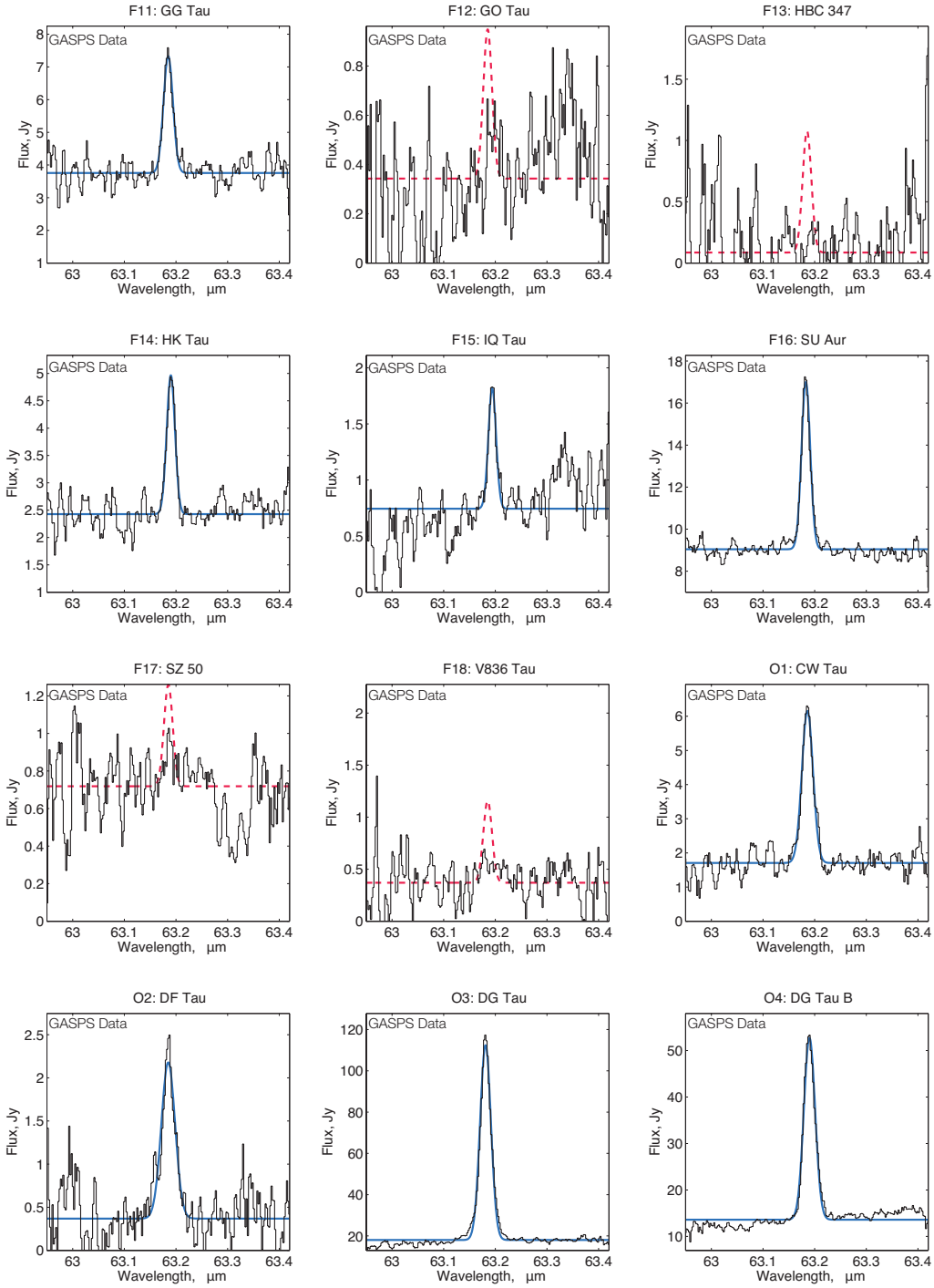

Fig. 7.— continued.

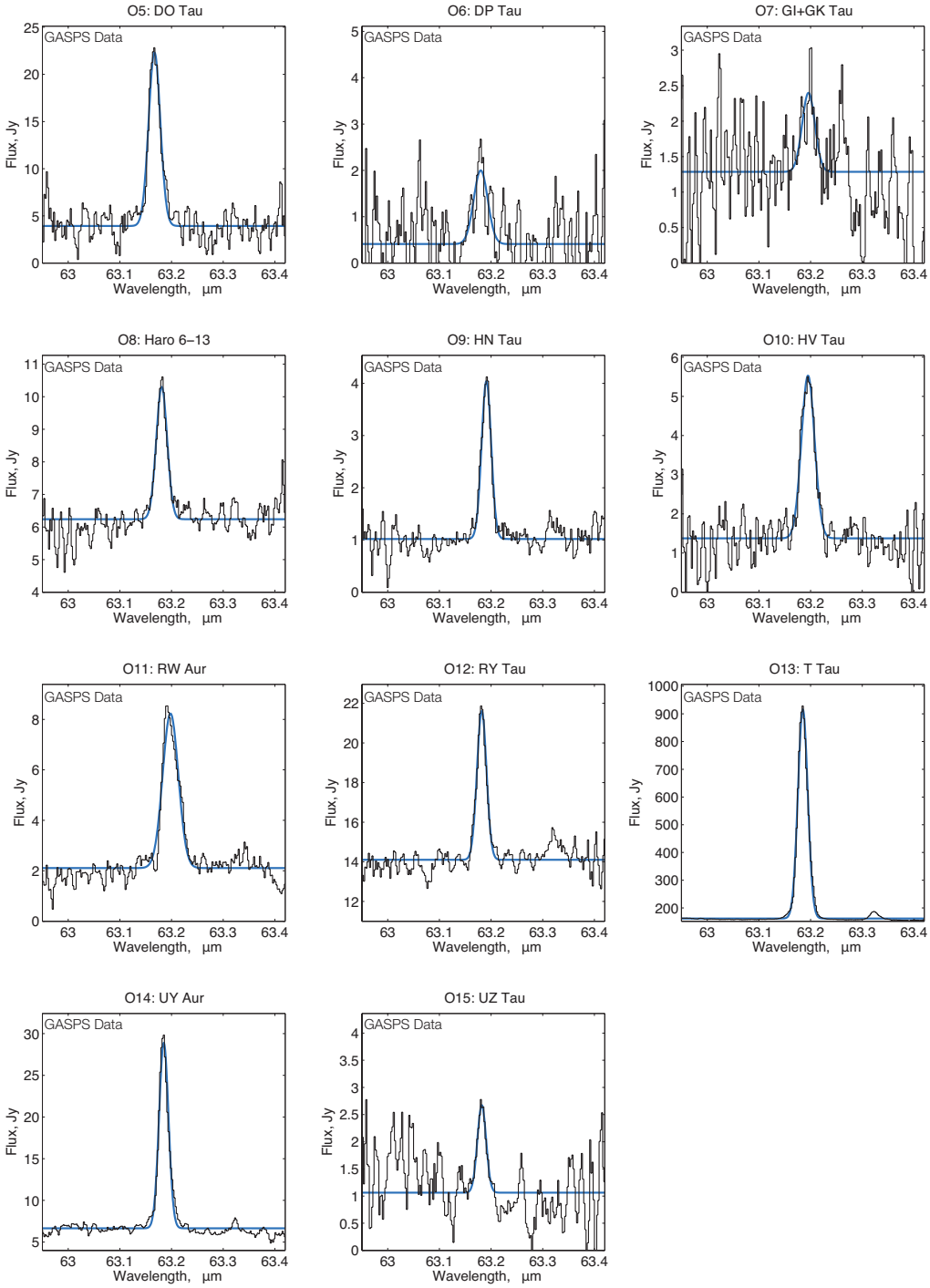

Fig. 7.— continued.

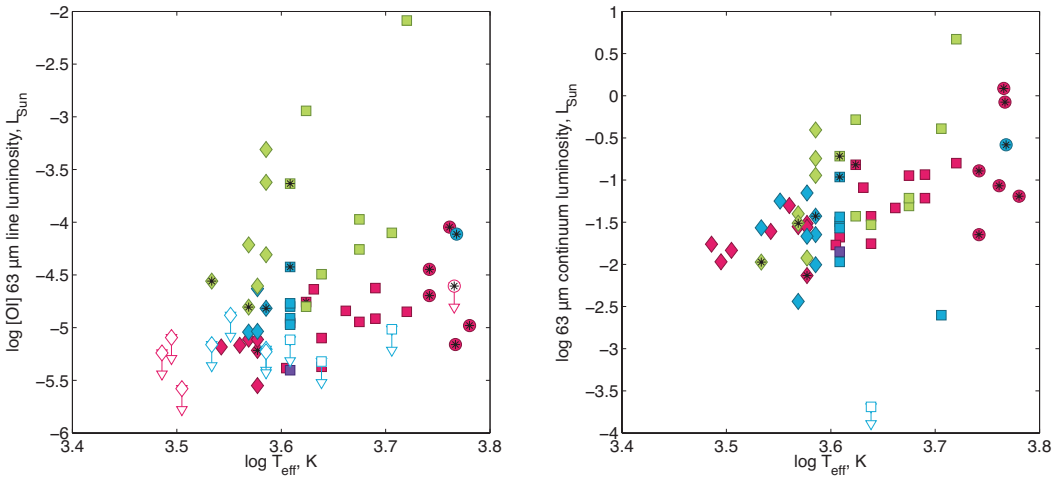

Fig. 8.— ONLINE ONLY. [OI] 63.18 μm line luminosity (left) and 63 μm continuum luminosity (right) vs effective temperature for our sample of transitional disks (red), full disks (blue), and outflow disks (green). 3σ upper limits are denoted by hollow data points with arrows. Symbols are as in *Figure 1a*.

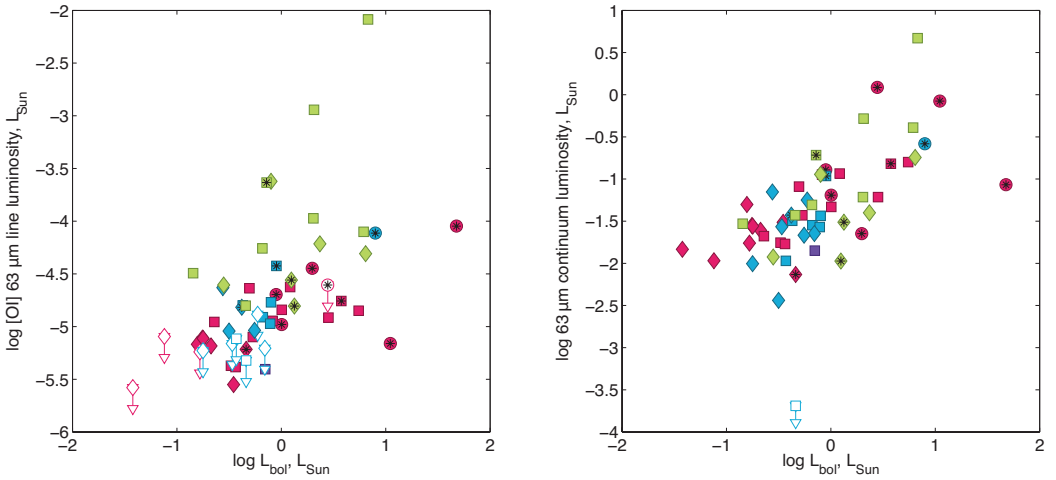

Fig. 9.— ONLINE ONLY. [OI] 63.18 μm line luminosity (left) and 63 μm continuum luminosity (right) vs bolometric luminosity for our sample of transitional disks (red), full disks (blue), and outflow disks (green). 3σ upper limits are denoted by hollow data points with arrows. Symbols are as in *Figure 1a*.

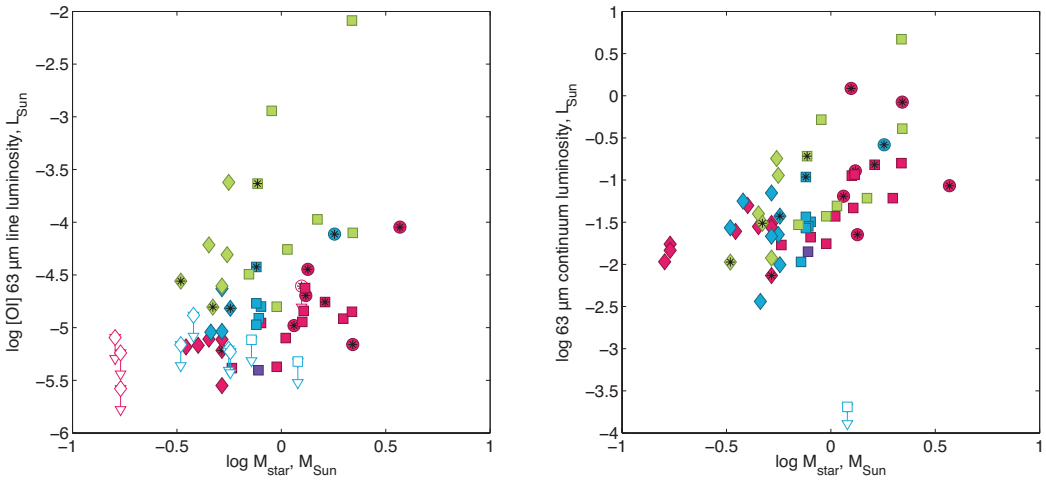

Fig. 10.— ONLINE ONLY. [OI] 63.18 μm line luminosity (left) and 63 μm continuum luminosity (right) vs stellar mass for our sample of transitional disks (red), full disks (blue), and outflow disks (green). 3σ upper limits are denoted by hollow data points with arrows. Symbols are as in *Figure 1a*.

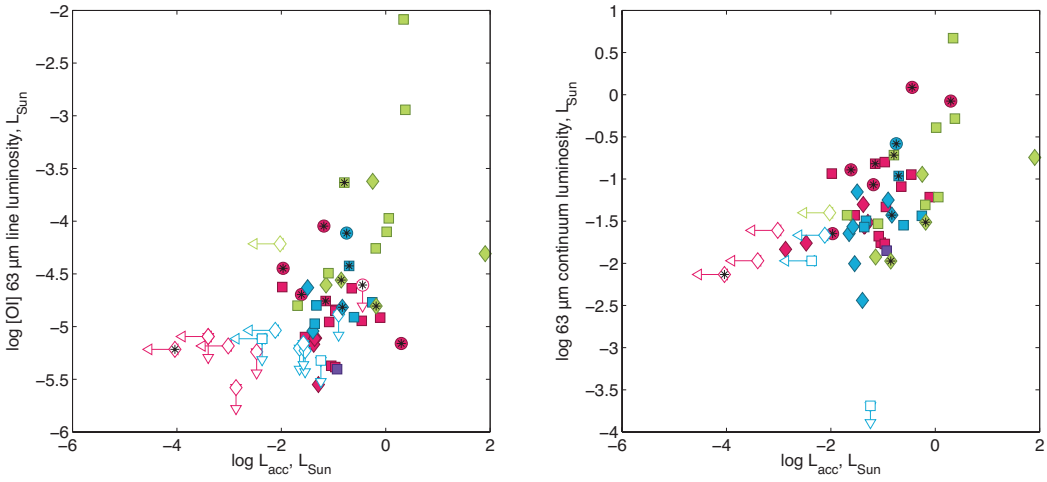

Fig. 11.— ONLINE ONLY. [OI] 63.18 μm line luminosity (left) and 63 μm continuum luminosity (right) vs accretion luminosity for our sample of transitional disks (red), full disks (blue), and outflow disks (green). 3σ upper limits are denoted by hollow data points with arrows. Symbols are as in *Figure 1a*.

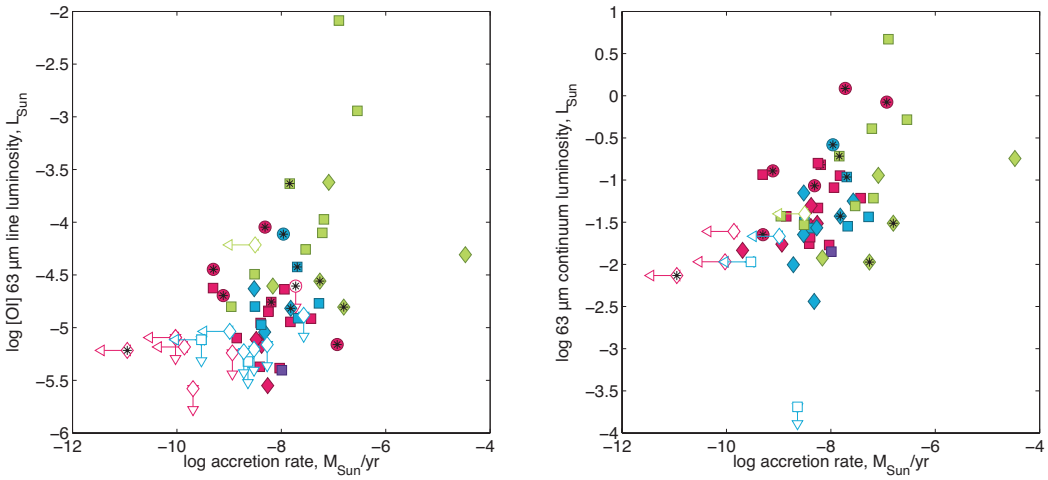
log [OI] 63 µm line luminosity, L_Sun
log accretion rate, M_Sun/yr
log 63 µm continuum luminosity, L_Sun
log accretion rate, M_Sun/yr

Fig. 12.— ONLINE ONLY. [OI] 63.18 μm line luminosity (left) and 63 μm continuum luminosity (right) vs accretion rate for our sample of transitional disks (red), full disks (blue), and outflow disks (green). 3σ upper limits are denoted by hollow data points with arrows. Symbols are as in *Figure 1a*.

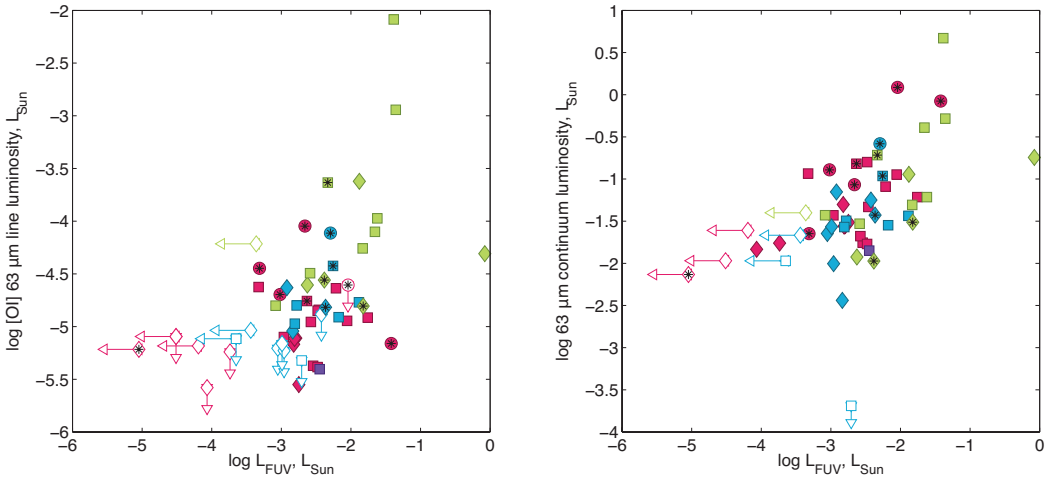

Fig. 13.— ONLINE ONLY. [OI] 63.18 μm line luminosity (left) and 63 μm continuum luminosity (right) vs FUV excess for our sample of transitional disks (red), full disks (blue), and outflow disks (green). 3σ upper limits are denoted by hollow data points with arrows. Symbols are as in *Figure 1a*.

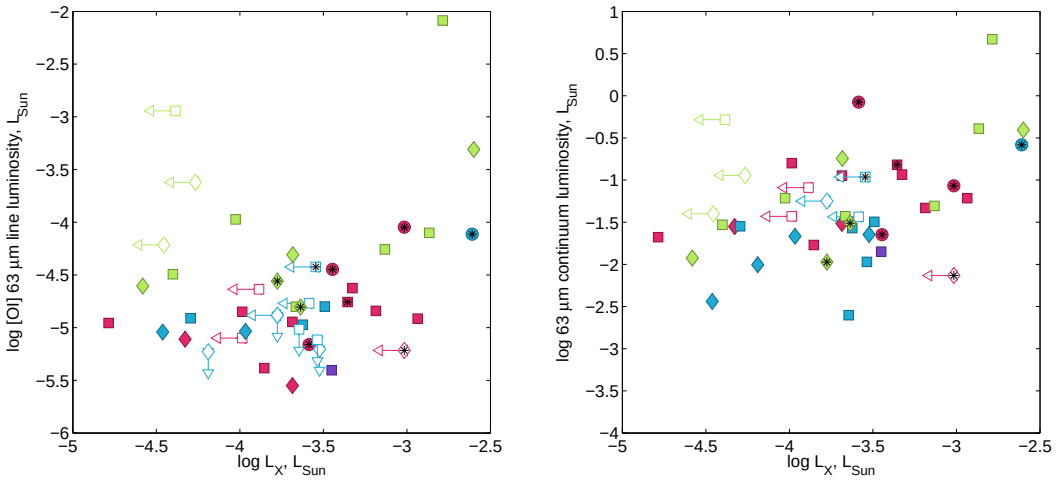

Fig. 14.— ONLINE ONLY. [OI] 63.18 μm line luminosity (left) and 63 μm continuum luminosity (right) vs X-ray luminosity for our sample of transitional disks (red), full disks (blue), and outflow disks (green). 3σ upper limits are denoted by hollow data points with arrows. Symbols are as in *Figure 1a*.

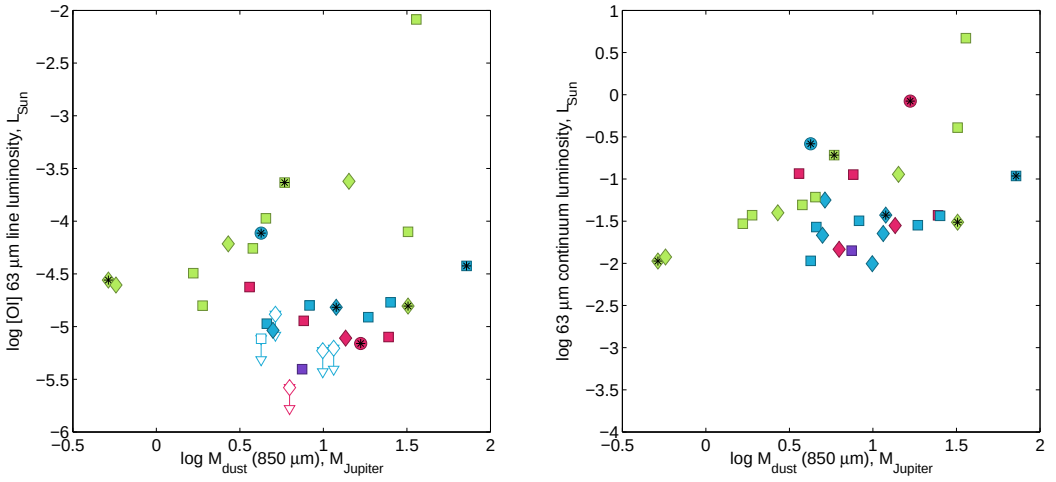

Fig. 15.— ONLINE ONLY. [OI] 63.18 μm line luminosity (left) and 63 μm continuum luminosity (right) vs dust mass (derived from 850 μm photometry) for our sample of transitional disks (red), full disks (blue), and outflow disks (green). 3σ upper limits are denoted by hollow data points with arrows. Symbols are as in *Figure 1a*.

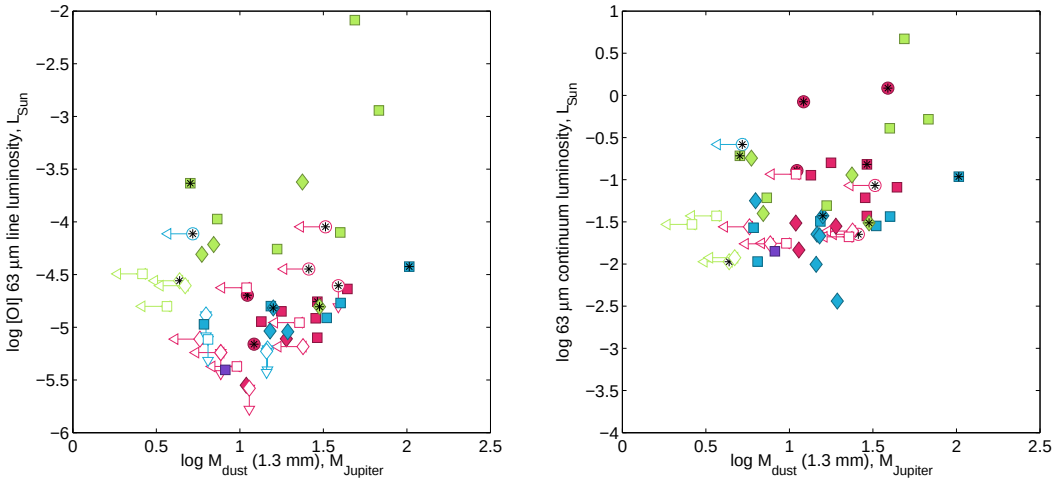

Fig. 16.— ONLINE ONLY. [OI] 63.18 μm line luminosity (left) and 63 μm continuum luminosity (right) vs dust mass (derived from 1.3 mm photometry) for our sample of transitional disks (red), full disks (blue), and outflow disks (green). 3σ upper limits are denoted by hollow data points with arrows. Symbols are as in *Figure 1a*.

TABLE 1

Herschel/PACS SAMPLE AND OBSERVATIONS

ID	Name	RA	Dec	Association	SpTy	Ref	Multiplicity	Ref	OBSID	Duration [s]
				Transition disks						
T1	16201-2410F-1*	16 23 09.23	-24 17 04.70	Ophiuchus	G0	F09	1	—	1342250127	8212
T2	CHX 22*	11 12 42 69	-77 22 23.00	Chameleon	G8	L07	2	D13	1342233474	8212
T3	CHX 7*	11 06 15 41	-77 21 56.90	Chameleon	G5	L07	—	—	1342233477	8212
T4	CR Cha	10 59 06 99	-77 01 40.40	Chameleon	K2	E11	2	G07	1342232614	8212
T5	CS Cha*	11 02 24 91	-77 33 35.70	Chameleon	K6	E11	—	—	1342233480	8212
T6	DM Tau	04 33 48.72	+18 10 09.99	Taurus	M1	KH95	—	—	1342225825⋆	6628
T7	DoAr 28	16 26 47.42	-23 14 52.20	Ophiuchus	K5	M92	—	—	1342241707	8212
T8	DoAr 44	16 31 33.46	-24 27 37.30	Ophiuchus	K3	M92	—	—	1342250578	8212
T9	GM Aur	04 55 10.99	+30 21 59.25	Taurus	K5.5	E11	—	—	1342191357⋆	1252
T10	Hn 24*	13 04 55 75	-77 39 49.50	Chameleon	M0.5	M10	2	B96	1342235656	8212
T11	LkCa 15	04 39 17.80	+22 21 03.48	Taurus	K5	KH95	—	—	1342225798⋆	6628
T12	LkHalpha 330*	3 45 48 28	+32 24 11.90	Perseus	G3	BR07	—	—	1342238377	8212
T13	RXJ1615.3-3255	16 15 20 23	-32 55 05.10	Lupus	K4	M10	—	—	1342229825	8212
T14	SSTLup	16 10 29.60	-39 22 15.00	Lupus	M5	M10	—	—	1342241709	8212
T15	Sz 111	16 08 54 69	-39 37 43.10	Lupus	M1.5	H94	—	—	1342220928	8212
T16	Sz 18	11 07 19 15	-76 03 04.80	Chameleon	M2.5	L07	—	—	1342232585	8212
T17	Sz 27	11 08 39 05	-77 16 04.20	Chameleon	K8	L07	—	—	1342233476	8212
T18	Sz 45	11 17 37 01	-77 04 38.10	Chameleon	M0.5	L07	—	—	1342233475	8212
T19	Sz 84	15 58 02 53	-37 36 02.70	Lupus	M5.5	M10	—	—	1342229826	8212
T20	Sz 91	16 07 11 61	-39 03 47.10	Lupus	M0.5	H94	—	—	1342229827	8212
T21	Sz Cha	10 58 16 77	-77 17 17.10	Chameleon	K0	E11	2	D13	1342233478	8212
T22	T Cha*	11 57 13 53	-79 21 31.50	Chameleon	G8	BR07	—	—	1342232294	2068
T23	TW Hya	11 01 52 03	-34 42 18.60	TW Hydra	K6	R06	—	—	1342187127⋆	1252
T24	UX Tau	04 30 03.76	+18 13 49.88	Taurus	K2	KH95	3	M06	1342214357⋆	1252
T25	WSB60	16 28 16.51	-24 36 58.00	Ophiuchus	M4.5	WMRG05	—	—	1342250128	8212
T26	YLW8*	16 27 10 28	-24 19 12.70	Ophiuchus	G2.5	BR07	2	M06	1342229824	2068
				Full disks						
F1	AA Tau	04 34 55.42	+24 28 53.16	Taurus	K7	KH95	—	—	1342225758⋆	6628
F2	BP Tau*	04 19 15.84	+29 06 26.94	Taurus	K7	KH95	—	—	1342225728⋆	3316
F3	CI Tau	04 33 52.00	+22 50 30.18	Taurus	K7	KH95	—	—	1342192125⋆	1252
F4	CY Tau	04 17 33.73	+28 20 46.85	Taurus	M1	KH95	—	—	1342192794⋆	1252
F5	DE Tau	04 21 55.64	+27 55 06.06	Taurus	M2	KH95	—	—	1342192797⋆	1252
F6	DK Tau	12 53 17.23	-77 07 10.70	Taurus	K7	KH95	2	WG01	1342225732⋆	3316
F7	DL Tau	04 33 39.06	+25 20 38.23	Taurus	K7	KH95	—	—	1342225800⋆	6628
F8	DN Tau	04 35 27.37	+24 14 58.94	Taurus	M0	KH95	—	—	1342225757⋆	3316
F9	DQ Tau*	04 46 53.04	+17 00 00.50	Taurus	M0	KH95	2	AW05	1342225806⋆	1252
F10	DS Tau	04 47 48.21	29 25 13.83	Taurus	K5	KH95	2	AW05	1342225851⋆	3316
F11	GG Tau*	04 32 30.35	+17 31 40.60	Taurus	K7	KH95	2	WG01	1342192121⋆	1252

TABLE 1—*Continued*

ID	Name	RA	Dec	Association	SpTy	Ref	Multiplicity	Ref	OBSID	Duration [s]
F12	GO Tau	04 43 03.10	+25 20 18.75	Taurus	M0	KH95	—	—	1342225826⋆	3316
F13	HBC 347	03 29 38.24	+24 30 37.74	Taurus	—	—	—	—	1342192136⋆	1252
F14	HK Tau	04 31 50.67	+24 24 17.44	Taurus	M0.5	KH95	2	WG01	1342225736⋆	3316
F15	IQ Tau	04 29 51.56	+26 06 44.89	Taurus	M0.5	KH95	—	—	1342225733⋆	3316
F16	SU Aur	04 55 59.38	+30 34 01.56	Taurus	G2	KH95	—	—	1342217844⋆	3316
F17	SZ 50	13 00 55.36	-77 10 22.10	Chameleon	M3	HH92	—	—	1342226008⋆	3316
F18	V836 Tau	05 03 06.60	+25 23 19.71	Taurus	K7	KH95	—	—	1342227634⋆	3316
				Outflow disks						
O1	CW Tau	04 14 17.00	+28 10 57.83	Taurus	K3	KH95	—	—	1342216221⋆	1252
O2	DF Tau*	04 27 02.80	+25 42 22.30	Taurus	M3	KH95	2	P08	1342190359⋆	1252
O3	DG Tau	04 27 04.698	+26 06 16.31	Taurus	K6	KH95	—	—	1342190382⋆	1252
O4	DG Tau B	04 27 02.41	+26 05 31.76	Taurus	M0	KH95	—	—	1342192798⋆	1252
O5	DO Tau	04 38 28.58	+26 10 49.44	Taurus	M0	KH95	—	—	1342190385⋆	1252
O6	DP Tau	04 42 37.56	+25 15 39.62	Taurus	M0.5	KH95	—	—	1342191362⋆	1252
O7	GI/GK Tau	04 55 10.85	+30 22 01.69	Taurus	K6	KH95	2	AW05	1342225760⋆	1252
O8	Haro 6-13	04 32 15.41	+24 28 59.75	Taurus	M0	RM12	—	—	1342192128⋆	1252
O9	HN Tau	04 33 39.44	+17 51 52.24	Taurus	K5	KH95	2	WG01	1342225796⋆	3316
O10	HV Tau	04 38 35.38	+26 10 37.80	Taurus	M1	KH95	2	WG01	1342225801⋆	3316
O11	RW Aur	05 07 49.41	+30 24 07.65	Taurus	K3	KH95	2	WG01	1342191359⋆	1252
O12	RY Tau	04 21 57.40	+28 26 35.54	Taurus	K1	KH95	—	—	1342190361⋆	1252
O13	T Tau	04 21 59.30	+19 32 08.53	Taurus	K0	KH95	2	WG01	1342190353⋆	1252
O14	UY Aur *	04 51 47.15	+30 47 14.44	Taurus	K7	KH95	2	WG01	1342215699⋆	1252
O15	UZ Tau*	04 32 42.73	+25 52 35.00	Taurus	M1	KH95	4	WG01	1342192131⋆	1252

NOTE.—Targets tagged with an asterisks were excluded from statistical tests due to either being a binary that does not meet the criteria in Sect. 2.1, or having a spectral type earlier than K-type. BP Tau was also excluded from statistical tests, due to its nature as an "evolved" full disk. OBSIDs tagged with a star (⋆) were observed by the GASPS team, and were previously reported in Howard et al. (2013), Meeus et al. (2012), and Podio et al. (2012), although they were re-reduced here using an updated version of the Herschel pipeline. Distances for each star forming association (from Reipurth et al. 2003): Chameleon, 160 pc; Lupus, 155 pc; Ophiuchus, 120 pc; Perseus, 250 pc; Taurus, 140 pc; TW Hya, 56 pc. References: Andrews and Williams 2005 (AW05), Brandner et al. 1996 (B96), Brown et al. 2007 (BR07), Daemgen et al. 2013 (D13), Espaillat et al. 2011 (E11), Furlan et al. 2009 (F09), Guenther et al. 2007 (G07), Hughes et al. 1994 (H94), Kenyon and Hartmann 1995 (KH95), Luhman 2007 (L07), Magazzu et al. 1992 (M92), McCabe et al. 2006 (M06), Merin et al. 2010 (M10), Pascucci et al. 2008 (P08), Riaz et al. 2006 (R06), White and Ghez 2001 (WG01), Wilking et al. 2005 (WMRG05).

TABLE 2
LITERATURE DATA

ID	R_{mag}	Ref	I_{mag}	Ref	A_V	Ref	Hα EW [Å]	Ref	log L_X [$L_\odot$]	Ref
Transition disks										
T1	14.20	C03	12.88	DENIS	6.90	MFM10	—	—	—	—
T2	10.45	GS92	10.02	GS92	1.21	GS92	1.5	GS92	-3.45	FK89
T3	10.28	GS92	7.64	GS92	3.39	GS92	1.2	B08	-3.02	FK89
T4	10.46	GS92	9.73	GS92	1.50	E11	38.1	GE97	-2.94	FK89
T5	10.92	GS92	9.11	GS92	0.85	GS92	13.3	GS92	-3.36	FK89
T6	12.92	KH95	11.77	KH95	0.00	KH95	138.7	CK79	-4.33	G07
T7	12.10	C03	11.69	DENIS	2.10	CMLW95	36	M92	—	—
T8	11.70	BA92	10.80	BA92	2.20	A11	68.3	BA92	-3.69	A11
T9	11.20	B93	10.70	B93	0.14	KH95	96.5 109 71	CK79, E94, C90	$\leq$ -3.89	A11
T10	13.00	C03	11.95	S07	2.00	M10	0.2	M10	$\leq$ -3.02	A00
T11	11.58	KH95	10.79	KH95	0.62	KH95	18.05	SB09	$\leq$ -3.99	A11
T12	11.20	C03	10.80	F95	1.55	OB95	16	SB09	—	—
T13	11.28	M10	10.54	M10	1.00	M10	26	M10	-3.19	A11
T14	15.79	M10	13.90	M10	1.00	M10	18	M10	—	—
T15	13.34	M08	12.17	M03	0.10	H94	145.2	H94	—	—
T16	14.15	GS92	12.69	GS92	1.60	E11	5	L04	—	—
T17	14.96	GS92	13.41	GS92	3.50	E11	100	L04	-4.79	W00
T18	12.57	GS92	11.59	GS92	0.60	E11	56	L04	-3.69	W00
T19	14.53	M10	12.94	M10	0.50	M10	44	M10	—	—
T20	14.28	H94	12.92	H94	2.00	H94	95.9	H94	—	—
T21	11.21	GS92	9.25	GS92	1.88	GS92	12	GS92	-3.99	F93
T22	11.07	S09	10.28	DENIS	1.70	S09	7.8	S09	—	—
T23	11.40	DENIS	9.38	DENIS	1.00	K99	213.8	R06	-3.85	H07
T24	10.48	KH95	9.75	KH95	0.21	KH95	3.9	T09	-3.33	D95
T25	16.55	WMRG05	14.33	DENIS	2.00	WMRG05	81	WMRG05	—	—
T26	12.20	DENIS	11.29	DENIS	9.00	PGS03	4	SB09	-3.59	A11
Full disks										
F1	12.06	KH95	10.99	HHG94	0.49	KH95	37.1 80 21	CK79, E94, C90	-3.49	G07
F2	11.31	KH95	10.45	KH95	0.49	KH95	40.1 55 47 49.4	CK79, E94, C90, MCH01	-3.45	G07
F3	12.22	KH95	11.12	KH95	1.77	KH95	102.1 64	CK79, C90	-4.30	G07
F4	12.35	KH95	11.18	KH95	0.10	KH95	69.5	CK79	-4.46	G07
F5	11.66	KH95	10.75	HHG94	0.59	KH95	54 76	CK79, C90	$\leq$ -3.78	D95
F6	11.43	KH95	10.46	KH95	0.76	KH95	19.4 13 28	CK79, E94, C90	-3.62	G07
F7	11.85	KH95	10.89	KH95	1.70	HEG95	105 111 138	WG01, CK79 C90	$\leq$ -3.59	D95
F8	11.49	KH95	10.49	KH95	0.49	KH95	11.9 22 15 11.1	CK79, E94, C90, MCH01	-3.52	G07
F9	12.40	KH95	11.27	KH95	0.97	KH95	112.9	CK79	—	—
F10	11.56	KH95	10.80	KH95	0.31	KH95	38.5	K98	—	—
F11	11.31	WG01	10.44	WG01	1.03	WG01	56 43 52	WG01, CK79, C90	$\leq$ -3.55	D95
F12	13.62	KH95	12.30	KH95	1.18	KH95	80.8	CK79	-4.19	G07
F13	—	—	—	—	—	—	—	—	-3.65	D95
F14	13.93	KH95	12.37	KH95	2.32	KH95	53.5	K98	—	—
F15	12.28	KH95	11.11	KH95	1.25	KH95	7.8	CK79	-3.97	G07
F16	8.62	KH95	8.10	KH95	0.90	KH95	3.5 5	CK79, C90	-2.61	G07
F17	14.30	HH92	12.50	HH92	2.14	HH92	66 46	SA11, CK79	—	—
F18	12.17	KH95	11.19	KH95	0.59	KH95	9 5	B90, C90	-3.54	N95
Outflow disks										
O1	12.33	KH95	11.42	KH95	2.29	KH95	137.9	R10	-3.13	G07
O2	11.07	KH95	9.87	KH95	0.21	KH95	53.9	CK79	-3.78	D95
O3	11.51	KH95	10.54	KH95	3.20	HEG95	112.8 73 110	CK79, E94, C90	$\leq$ -4.39	—
O4	—	—	—	—	—	—	—	—	-2.60	G07

TABLE 2—*Continued*

ID	R_{mag}	Ref	I_{mag}	Ref	A_V	Ref	Hα EW [Å]	Ref	log L_X [$L_\odot$]	Ref
O5	12.41	KH95	11.37	HHG94	2.64	KH95	108.9 101	CK79, C90	$\leq$ -4.27	B99
O6	13.09	KH95	11.95	KH95	1.46	KH95	85.4	CK79	-4.58	G07
O7	12.15	KH95	11.06	KH95	0.87	KH95	22.5 17	K98, CK79	-3.66	G07
O8	14.85	KGW08	13.54	L00	11.90	K09	88.2	CK79	-3.68	G07
O9	12.96	KH95	12.17	KH95	0.52	KH95	158	E87	-4.40	G07
O10	12.68	KH95	9.87	KH95	1.91	KH95	8.5	E87	$\leq$ -4.46	N95
O11	9.95	KH95	9.34	KH95	0.50	F09	84.2	CK79	-4.03	D95
O12	9.53	KH95	8.80	KH95	1.84	KH95	21	B90	-2.87	G07
O13	9.19	KH95	8.50	KH95	1.39	KH95	38	T09	-2.79	C98
O14	11.92	KH95	10.83	KH95	1.35	KH95	47 72.8	E87, CK79	—	—
O15	11.20	KH95	10.28	M03	1.49	KH95	73.5 98.1	E87, CK79	-3.64	G07

NOTE.—References: Alcala et al. 2000 (A00), Andrews et al. 2011 (A11), Antoniucci et al. 2011 (SA11), Bary et al. 2008 (B08), Beckwith et al. 1990 (B90), Bouvier and Appenzeller, 1992 (BA92), Bouvier et al. 1993 (B93), Briceño et al. 1999 (B99), Cabrit et al. 1990 (C90), Carkner et al. 1998 (C98), Chen et al. 1995 (CMLW95), Cohen and Kuhi 1979 (CK79), Cutri et al. 2003 (C03), Damiani et al. 1995 (D95), DENIS Consortium 2005 (DENIS), Edwards et al. 1987 (E87), Edwards et al. 1994 (E94), Espaillat et al. 2011 (E11), Feigelson and Kriss 1989 (FK89), Feigelson et al. 1993 (F93), Fernandez, 1995 (F95), Furlan et al. 2009 (F09), Gauvin and Strom 1992(GS92), Gudel et al. 2007 (G07), Guenther and Emerson, 1997 (GE97), Hartigan, Edwardds, and Ghandour 1995 (HEG95), Herbst et al. 1994 (HHG94), Herczeg et al. 2007 (H07), Hughes et al. 1994 (H94), Kastner et al. 1999 (K99), Kenyon and Hartmann 1995 (KH95), Kenyon et al. 1998 (K98), Kenyon, Gomez, and Whitney, 2008 (KGW08), Kraus & Hillenbrand 2009 (K09), Luhman 2000 (L00), Luhman 2004 (L04), Magazzu et al. 1992 (M92), McClure et al. 2010 (MFM10), Merin et al. 2010 (M10), Monet, 2003 (M03), Muzerolle, Calvet, and Hartmann 2001(MCH01), Neuhauser et al. 1995 (N95), Osterloh and Beckwith, 1995 (OB95), Prato, Greene, Simon, 2003 (PGS03), Rebull et al. 2010 (R10), Riaz et al. 2006 (R06), Salyk et al. 2009 (SB09), Schisano et al. 2009 (S09), Spezzi et al. 2007 (S07), Taguchi et al. 2009 (T09), White and Ghez 2001 (WG01), White et al. 2000 (W00), Wilking et al. 2006 (WMRG05).

TABLE 3
STELLAR AND ACCRETION PROPERTIES

ID	T_{eff} [K]	$M_\star$ [$M_\odot$]	L_{bol} [$L_\odot$]	$R_\star$ [$R_\odot$]	log L_{acc} [$L_\odot$]	log $\dot{M}$ [$M_\odot$/yr]	log L_{FUV} [$L_\odot$]
				Transition disks			
T1	6030	1.15	1.01	0.92	—	—	—
T2	5520	1.34	1.98	1.54	-2.0	-9.3	-3.3
T3	5770	3.7	47.60	6.92	-1.2	-8.3	-2.7
T4	4900	1.98	2.83	2.34	-0.1	-7.4	-1.8
T5	4205	1.62	3.76	3.66	-1.2	-8.2	-2.6
T6	3705	0.45	0.18	1.02	-1.3	-8.4	-2.8
T7	4350	0.95	0.33	1.01	-1.0	-8.4	-2.5
T8	4730	1.26	0.82	1.35	-0.5	-7.8	-2.1
T9	4277.5	1.00	0.50	1.28	-0.7	-7.9	-2.2
T10	3777.5	0.52	0.46	1.59	$\leq$ -4.0	$\leq$ -11.0	$\leq$ -5.0
T11	4350	1.05	0.53	1.29	-1.5	-8.9	-3.0
T12	5830	1.25	2.78	1.64	-0.4	-7.7	-2.0
T13	4590	1.28	1.01	1.59	-0.9	-8.2	-2.5
T14	3125	0.16	0.08	0.94	$\leq$ -3.4	$\leq$ -10.0	$\leq$ -4.5
T15	3632.5	0.40	0.16	1.00	-1.4	-8.4	-2.8
T16	3487.5	0.35	0.21	1.26	$\leq$ -3.0	$\leq$ -9.9	$\leq$ -4.2
T17	4060	0.80	0.23	0.97	-1.1	-8.4	-2.6
T18	3777.5	0.52	0.35	1.38	-1.3	-8.3	-2.7
T19	3060	0.17	0.17	1.45	-2.5	-8.9	-3.7
T20	3777.5	0.52	0.18	0.99	-1.4	-8.5	-2.8
T21	5250	2.18	5.50	2.84	-1.0	-8.2	-2.5
T22	5520	1.31	0.89	1.04	-1.6	-9.1	-3.0
T23	3850	0.58	0.39	1.40	-1.0	-8.0	-2.5
T24	4900	1.3	1.21	1.53	-2.0	-9.3	-3.3
T25	3197.5	0.17	0.04	0.64	-2.9	-9.7	-4.1
T26	5845	2.20	11.06	3.25	0.3	-6.9	-1.4
				Full disks			
F1	4060	0.8	0.43	1.32	-1.3	-8.5	-2.8
F2	4060	0.78	0.70	1.70	-0.9	-8.0	-2.4
F3	4060	0.78	0.67	1.65	-0.6	-7.7	-2.2
F4	3705	0.46	0.32	1.37	-1.4	-8.3	-2.8
F5	3560	0.38	0.59	2.03	-0.9	-7.6	-2.4
F6	4060	0.76	0.78	1.79	-1.4	-8.4	-2.8
F7	4060	0.76	0.80	1.81	-0.3	-7.3	-1.9
F8	3850	0.56	0.70	1.88	-1.7	-8.5	-3.0
F9	3850	0.57	0.42	1.46	-0.8	-7.8	-2.4
F10	4350	1.2	0.46	1.20	-1.2	-8.6	-2.7
F11	4060	0.76	0.90	1.92	-0.7	-7.7	-2.3
F12	3850	0.57	0.18	0.95	-1.5	-8.7	-3.0
F13	—	—	—	—	—	—	—
F14	3777.5	0.52	0.28	1.23	-1.5	-8.5	-2.9
F15	3777.5	0.52	0.55	1.74	-2.1	-9.0	-3.4
F16	5860	1.8	7.96	2.74	-0.7	-8.0	-2.3
F17	3415	0.33	0.34	1.67	-1.6	-8.3	-3.0
F18	4060	0.72	0.37	1.23	$\leq$ -2.4	$\leq$ -9.5	$\leq$ -3.6
				Outflow disks			
O1	4730	1.07	0.66	1.21	-0.2	-7.5	-1.8
O2	3415	0.33	1.25	3.20	-0.9	-7.3	-2.4
O3	4205	0.9	2.06	2.71	0.4	-6.5	-1.4
O4	3850	—	—	—	—	—	—

TABLE 3—*Continued*

ID	T_{eff} [K]	$M_\star$ [$M_\odot$]	L_{bol} [$L_\odot$]	$R_\star$ [$R_\odot$]	log L_{acc} [$L_\odot$]	log $\dot{M}$ [$M_\odot$/yr]	log L_{FUV} [$L_\odot$]
O5	3850	0.56	0.80	2.01	-0.2	-7.1	-1.9
O6	3777.5	0.52	0.28	1.24	-1.1	-8.2	-2.6
O7	4205	0.95	0.46	1.27	-1.7	-9.0	-3.1
O8	3850	0.55	6.42	5.71	1.9	-4.5	-0.1
O9	4350	0.7	0.14	0.67	-1.1	-8.5	-2.6
O10	3705	0.45	2.34	3.72	$\leq$ -2.0	$\leq$ -8.5	$\leq$ -3.4
O11	4730	1.49	2.03	2.13	0.1	-7.2	-1.6
O12	5080	2.2	6.15	3.21	0.0	-7.2	-1.7
O13	5250	2.18	6.77	3.15	0.3	-6.9	-1.4
O14	4060	0.77	0.72	1.72	-0.8	-7.8	-2.3
O15	3705	0.47	1.34	2.81	-0.2	-6.8	-1.8

TABLE 4
DISK PROPERTIES

ID	r_{gap} [AU]	Ref	h_{wall} [AU]	Ref	$f_{850\mu m}$ [mJy]	$f_{1.3mm}$ [mJy]	Ref	$M_{850\mu m}$ [M_{Jup}]	$M_{1.3mm}$ [M_{Jup}]
Transition disks									
T1			—	—	—	—	—	—	—
T2	37.1	KM09	—	—	—	$\leq$ 118	H93	—	$\leq$ 25.8
T3	146.7	KM09	—	—	—	$\leq$ 143	H93	—	$\leq$ 32.5
T4	10	E11	—	—	—	124.9	H93	—	28.4
T5	38	E11	7	E11	—	128.4	H93	—	29.1
T6	19	A11	5.7	A11	237	109	M13	13.6	19.0
T7	—	—	—	—	—	$\leq$ 75	M13	—	$\leq$ 9.6
T8	30	A11	9	A11	181	105	M13	7.6	13.4
T9	23	E11	2.9	E11	—	253	M13	—	44.1
T10	—	—	—	—	—	—	—	—	—
T11	39	E11	5	E11	428	167	M13	24.5	29.1
T12	68	A11	6.8	A11	—	70	OB95	—	38.9
T13	30	A11	2	A11	—	—	—	—	—
T14	—	—	—	—	—	—	—	—	—
T15	—	—	—	—	—	—	—	—	—
T16	13	E11	2	E11	—	105	H93	—	23.9
T17	5	E11	4	E11	—	100	H93	—	22.8
T18	20	E11	4	E11	—	47.8	H93	—	10.9
T19	55	M10	—	—	—	$\leq$ 36	N97	—	$\leq$ 7.7
T20	—	—	—	—	—	$\leq$ 27	N97	—	$\leq$ 5.8
T21	18	E11	4	E11	—	77.5	H93	—	17.7
T22	15	BR07	—	—	—	105.2	H93	—	11.1
T23	4	T10	—	—	—	—	—	—	—
T24	—	—	—	—	$\leq$ 173	$\leq$ 63	M13	$\leq$ 3.6	$\leq$ 11.0
T25	15	A11	0.8	A11	149	89	M13	6.3	11.4
T26	36	A11	8.2	A11	397	95	M13	16.7	12.2
Full disks									
F1	—	—	—	—	144	88	M13	8.3	15.3
F2	—	—	—	—	130	47	M13	7.5	8.2
F3	—	—	—	—	324	190	M13	18.6	33.1
F4	—	—	—	—	—	111	G11		19.3
F5	—	—	—	—	90	36	M13	5.2	6.3
F6	—	—	—	—	80	35	M13	4.6	6.1
F7	—	—	—	—	440	230	M13	25.2	40.1
F8	—	—	—	—	201	84	M13	11.5	14.6
F9	—	—	—	—	208	91	M13	11.9	15.9
F10	—	—	—	—	—	—	—	—	—
F11	—	—	—	—	1255	593	M13	72.0	103.3
F12	—	—	—	—	173	83	M13	9.9	14.5
F13	—	—	—	—	—	—	—	—	—
F14	—	—	—	—	—	—	—	—	—
F15	—	—	—	—	178	87	M13	5.0	15.2
F16	—	—	—	—	74	$\leq$ 30	M13	4.2	$\leq$ 5.2
F17	—	—	—	—	—	—	—	—	—
F18	—	—	—	—	74	37	M13	4.2	6.4
Outflow disks									
O1	—	—	—	—	66	96	M13	3.8	16.7
O2	—	—	—	—	8.8	$\leq$ 25	M13	0.5	$\leq$ 4.4
O3	—	—	—	—	—	389.9	G11	—	67.9
O4	—	—	—	—	—	—	—	—	—

TABLE 4—*Continued*

ID	r_{gap} [AU]	Ref	h_{wall} [AU]	Ref	$f_{850\mu m}$ [mJy]	$f_{1.3mm}$ [mJy]	Ref	$M_{850\mu m}$ [M_{Jup}]	$M_{1.3mm}$ [M_{Jup}]
O5	—	—	—	—	248	136	M13	14.2	23.7
O6	—	—	—	—	≤ 10	≤ 27	M13	≤ 0.6	≤ 4.7
O7	—	—	—	—	33	≤ 21	M13	1.9	≤ 3.7
O8	—	—	—	—	—	34.2	G11	—	5.9
O9	—	—	—	—	29	≤ 15	M13	1.7	≤ 2.6
O10	—	—	—	—	47	40	A05	2.7	7.0
O11	—	—	—	—	79	42	M13	4.5	7.3
O12	—	—	—	—	560	229	M13	32.1	39.9
O13	—	—	—	—	628	280	M13	36.0	48.8
O14	—	—	—	—	102	29	M13	5.9	5.1
O15	—	—	—	—	560	172	M13	32.1	30.0

NOTE.—References: Andrews and Williams 2005, and references therein (A05), Andrews et al. 2011 (A11), Brown et al. 2007 (BR07), Espaillat et al. 2011 (E11), Guilloteau et al. 2011 (G11), Henning et al. 1993 (H93), Kim et al. 2009 (KM09), Merin et al. 2010 (M10), Mohanty et al. 2013, and references therein (M13), Nurnberger et al. 1997 (N97), Osterloh and Beckwith, 1995 (OB95), Thi et al. 2010 (T10).

TABLE 5
Herschel PACS RESULTS

ID	[OI] 63.18 μm line flux (10^{-17} W/m^2)	o-H_2O 63.32 μm line flux (10^{-17} W/m^2)	63 μm continuum flux (Jy)
		Transition disks	
T1	2.340 ± 0.143	≤0.716	3.029 ± 0.010
T2	4.492 ± 0.200	≤ 1.192	0.596 ± 0.020
T3	11.284 ± 0.851	≤ 5.325	2.262 ± 0.055
T4	1.530 ± 0.150	≤ 0.658	1.618 ± 0.015
T5	2.200 ± 0.134	≤ 0.702	4.017 ± 0.010
T6	1.276 ± 0.305	≤ 0.960	0.972 ± 0.016
T7	0.949 ± 0.076	≤ 0.541	0.829 ± 0.013
T8	2.536 ± 0.189	1.014 ± 0.145	5.315 ± 0.012
T9	3.793 ± 0.513	≤ 2.435	2.810 ± 0.036
T10	0.764 ± 0.101	≤ 0.523	0.195 ± 0.008
T11	1.306 ± 0.165	≤ 0.770	1.285 ± 0.012
T12	≤ 1.276	≤ 1.276	13.239 ± 0.019
T13	1.934 ± 0.118	≤ 0.534	1.317 ± 0.009
T14	≤ 1.078	≤ 1.078	0.303 ± 0.016
T15	0.910 ± 0.112	≤ 0.540	1.406 ± 0.008
T16	0.823 ± 0.140	≤ 0.817	0.652 ± 0.012
T17	1.390 ± 0.124	≤ 0.755	0.556 ± 0.011
T18	0.354 ± 0.097	≤ 0.637	0.810 ± 0.008
T19	≤ 0.770	≤ 0.770	0.490 ± 0.013
T20	1.035 ± 0.112	≤ 0.730	0.779 ± 0.016
T21	1.777 ± 0.100	≤ 0.793	4.199 ± 0.008
T22	5.455 ± 0.291	≤ 1.493	7.318 ± 0.021
T23	4.239 ± 0.345	≤ 1.556	3.675 ± 0.024
T24	3.894 ± 0.266	≤ 1.671	4.021 ± 0.024
T25	≤ 0.590	≤ 0.590	0.690 ± 0.009
T26	1.543 ± 0.296	≤ 2.534	39.540 ± 0.023
		Full disks	
F1	2.606 ± 0.109	0.956 ± 0.131	1.106 ± 0.016
F2	0.647 ± 0.146	0.898 ± 0.173	0.490 ± 0.024
F3	2.016 ± 0.183	≤ 0.921	0.979 ± 0.014
F4	1.489 ± 0.416	≤ 1.573	0.126 ± 0.027
F5	0.712 ± 0.384	≤ 2.150	1.946 ± 0.039
F6	1.748 ± 0.155	0.455 ± 0.157	0.932 ± 0.012
F7	2.792 ± 0.208	0.640 ± 0.176	1.268 ± 0.012
F8	≤ 1.023	≤ 1.023	0.780 ± 0.015
F9	2.505 ± 0.351	≤ 1.413	1.292 ± 0.021
F10	≤ 0.782	≤ 0.782	≤ 0.037
F11	6.185 ± 0.381	≤ 1.850	3.756 ± 0.028
F12	≤ 0.969	≤ 0.969	0.343 ± 0.019
F13	≤ 1.585	≤ 1.585	0.086 ± 0.024
F14	3.847 ± 0.262	≤ 1.234	2.428 ± 0.023
F15	1.512 ± 0.256	0.968 ± 0.294	0.744 ± 0.019
F16	12.650 ± 0.336	≤ 1.474	9.043 ± 0.027
F17	≤ 0.866	≤ 0.866	0.719 ± 0.014
F18	≤ 1.259	≤ 1.259	0.370 ± 0.015
		Outflow disks	
O1	9.061 ± 0.364	≤ 1.601	1.707 ± 0.024
O2	4.541 ± 0.333	≤ 1.410	0.369 ± 0.035
O3	187.160 ± 3.075	≤ 10.125	18.015 ± 0.224

TABLE 5—*Continued*

ID	[OI] 63.18 μm line flux (10^{-17} W/m^2)	o-H_2O 63.32 μm line flux (10^{-17} W/m^2)	63 μm continuum flux (Jy)
O4	80.446 ± 1.891	≤ 6.355	13.600 ± 0.113
O5	39.268 ± 1.971	≤ 7.357	3.932 ± 0.129
O6	4.069 ± 1.085	≤ 3.880	0.411 ± 0.060
O7	2.592 ± 0.803	≤ 4.039	1.286 ± 0.057
O8	8.075 ± 0.397	≤ 2.109	6.240 ± 0.030
O9	5.272 ± 0.221	≤ 1.130	1.020 ± 0.017
O10	10.000 ± 0.548	≤ 2.385	1.376 ± 0.034
O11	17.452 ± 0.701	0.947 ± 0.320	2.109 ± 0.043
O12	13.020 ± 0.640	2.481 ± 0.740	14.103 ± 0.049
O13	1348.400 ± 14.564	46.876 ± 1.506	161.870 ± 0.966
O14	38.197 ± 0.828	1.660 ± 0.389	6.650 ± 0.058
O15	2.573 ± 0.554	≤ 2.789	1.062 ± 0.046

NOTE.—Detections are listed with ± 1-sigma uncertainties; 3-sigma upper limits are reported for non-detections.

TABLE 6
SUBSAMPLE CORRELATION TESTS

Correlation Test	Subsample Being Tested	Correlation Tests P(1)	P(2)	P(3)	Correlated?	Linear Regression Intercept	Slope
L 63 μm v. L [OI] 63 μm	All Objects	0.0%	0.0%	0.0%	**Correlated**	-3.24± 0.18	1.15 ± 0.13
	Transitional Disks Only	0.0%	0.0%	0.1%	**Correlated**	-4.07 ± 0.21	0.74 ± 0.15
	Full Disks Only	10.0%	0.7%	3.3%	**Correlated**	-4.42 ± 0.31	0.38 ± 0.18
	Outflow Disks Only	0.2%	0.2%	0.5%	**Correlated**	-3.01 ± 0.17	0.97 ± 0.15
T_{eff} v. L [OI] 63 μm	All Objects	0.1%	0.3%	0.4%	**Correlated**	-7.66 ± 0.93	0.0007 ± 0.0002
	Transitional Disks Only	0.0%	0.1%	0.2%	**Correlated**	-6.67 ± 0.39	0.0004 ± 0.0001
	Full Disks Only	82.7%	84.7%	87.3%	Not Correlated	-4.68 ± 1.15	-0.0001 ± 0.0003
	Outflow Disks Only	24.7%	29.7%	33.0%	Not Correlated	-6.22 ± 1.70	0.0005 ± 0.0004
T_{eff} v. L 63 μm	All Objects	10.9%	0.4%	1%	Not Correlated	-3.09 ± 0.73	0.0004 ± 0.0002
	Transitional Disks Only	0.0%	0.1%	0.2%	**Correlated**	-3.17 ± 0.30	0.0004 ± 0.0001
	Full Disks Only	10.4%	28.4%	18.0%	Not Correlated	1.81 ± 1.63	-0.0009 ± 0.0004
	Outflow Disks Only	11.8%	14.4%	15.6%	Not Correlated	-3.79 ± 1.45	0.0007 ± 0.0003
L_{bol} v. L [OI] 63 μm	All Objects	0.0%	0.0%	0.0%	**Correlated**	-4.61 ± 0.10	1.02 ± 0.19
	Transitional Disks Only	0.1%	0.3%	0.3%	**Correlated**	-4.96 ± 0.07	0.41 ± 0.11
	Full Disks Only	28.3%	45.7%	38.3%	Not Correlated	-4.94 ± 0.19	0.39 ± 0.50
	Outflow Disks Only	3.0%	7.3%	4.7%	**Correlated**	-4.04 ± 0.20	0.75 ± 0.35
L_{bol} v. L 63 μm	All Objects	0.0%	0.0%	0.0%	**Correlated**	-1.23± 0.09	0.78 ± 0.15
	Transitional Disks Only	0.0%	0.1%	0.2%	**Correlated**	-1.23 ± 0.06	0.52 ± 0.09
	Full Disks Only	29.0%	32.9%	36.9%	Not Correlated	-1.60 ± 0.39	0.64 ± 0.99
	Outflow Disks Only	0.2%	0.4%	0.8%	**Correlated**	-1.08± 0.14	0.97 ± 0.25
L_X v. L [OI] 63 μm	All Objects	5.9%	59.0%	80.7%	Not Correlated	-5.59 ± 0.50	-0.18 ± 0.13
	Transitional Disks Only	6.4%	56.9%	53.7%	Not Correlated	-5.62 ± 0.29	-0.14 ± 0.08
	Full Disks Only	65.5%	92.0%	—	Not Correlated	-5.35 ± 0.79	-0.06 ± 0.20
	Outflow Disks Only	9.1%	39.5%	54.8%	Not Correlated	-2.69 ± 0.64	0.40 ± 0.18
L_X v. L 63 μm	All Objects	3.0%	69.6%	13.9%	Not Correlated	-2.21 ± 0.36	-0.18 ± 0.10
	Transitional Disks Only	0.3%	37.1%	27.6%	Not Correlated	-2.32 ± 0.34	-0.24 ± 0.09
	Full Disks Only	86.4%	73.2%	80.9%	Not Correlated	-2.03 ± 0.58	-0.03 ± 0.15
	Outflow Disks Only	0.8%	8.9%	18.5%	Not Correlated	0.59 ± 0.53	0.47 ± 0.15
L_{acc} v. L [OI] 63 μm	All Objects	0.0%	0.0%	0.0%	**Correlated**	-4.22± 0.15	0.66 ± 0.12
	Transitional Disks Only	1.0%	4.7%	4.9%	**Correlated**	-4.76 ± 0.15	0.28 ± 0.11
	Full Disks Only	3.5%	17.6%	16.1%	Not Correlated	-4.69 ± 0.27	0.34 ± 0.22
	Outflow Disks Only	5.7%	5.2%	8.6%	Not Correlated	-3.88 ± 0.23	0.41 ± 0.22
L_{acc} v. L 63 μm	All Objects	0.0%	0.0%	0.0%	**Correlated**	-0.97± 0.14	0.47 ± 0.10
	Transitional Disks Only	0.3%	4.1%	2.8%	**Correlated**	-1.06 ± 0.14	0.29 ± 0.09
	Full Disks Only	3.6%	19.9%	18.2%	Not correlated	-1.21 ± 0.61	0.54 ± 0.44
	Outflow Disks Only	0.7%	1.6%	1.2%	**Correlated**	-0.85 ± 0.19	0.48 ± 0.18
$\dot{M}$ v. L [OI] 63 μm	All Objects	0.0%	0.1%	0.1%	**Correlated**	-0.44 ± 0.94	0.55 ± 0.12
	Transitional Disks Only	4.0%	13.5%	12.1%	Not Correlated	-3.03 ± 1.15	0.25 ± 0.14
	Full Disks Only	7.0%	36.8%	25.2%	Not Correlated	-2.68 ± 1.66	0.30 ± 0.20
	Outflow Disks Only	10.8%	1.5%	4.5%	**Correlated**	-1.91 ± 1.44	0.28 ± 0.19
$\dot{M}$ v. L 63 μm	All Objects	0.0%	0.0%	0.0%	**Correlated**	2.12 ± 0.81	0.44 ± 0.10
	Transitional Disks Only	0.6%	1.2%	2.5%	**Correlated**	1.24 ± 1.01	0.32 ± 0.12
	Full Disks Only	0.7%	4.4%	4.3%	**Correlated**	4.50 ± 3.29	0.77 ± 0.40
	Outflow Disks Only	1.2%	1.0%	1.0%	**Correlated**	1.56 ± 1.21	0.35 ± 0.16
m_{disk} v. L [OI] 63 μm	All Objects	0.0%	26.5%	43.6%	Not Correlated	-5.79 ± 0.25	0.04 ± 0.01
	Transitional Disks Only	0.3%	26.6%	20.0%	Not Correlated	-4.72 ± 0.18	0.03 ± 0.01
	Full Disks Only	1.9%	44.7%	8.2%	Not Correlated	-5.25 ± 0.13	0.01 ± 0.01
	Outflow Disks Only	0.0%	4.4%	2.3%	**Correlated**	-4.78 ± 0.26	0.03 ± 0.01
m_{disk} v. L 63 μm	All Objects	0.0%	5.7%	7.9%	**Correlated**	-2.14 ± 0.16	0.03 ± 0.01
	Transitional Disks Only	0.6%	7.7%	5.6%	**Correlated**	-2.13 ± 0.25	0.03 ± 0.01

TABLE 6—*Continued*

Correlation Test	Subsample Being Tested	Correlation Tests P(1)	P(2)	P(3)	Correlated?	Linear Regression Intercept	Slope
	Full Disks Only	6.6%	95.1%	86.7%	Not Correlated	-2.05 ± 0.20	0.02 ± 0.01
	Outflow Disks Only	0.0%	4.4%	13.0%	**Correlated**	-1.71 ± 0.24	0.03 ± 0.01
a_{cavity} v. L [OI] 63 μm	Transitional Disks Only	71.1%	77.0%	69.5%	Not Correlated	-5.10 ± 0.17	-0.0012 ± 0.01
a_{cavity} v. L 63 μm	Transitional Disks Only	75.0%	24.6%	26.5%	Not Correlated	-1.46 ± 0.16	0.00 ± 0.01
h_{wall} v. L [OI] 63 μm	Transitional Disks Only	23.6%	78.5%	64.7%	Not Correlated	-5.25 ± 0.20	0.04 ± 0.04
h_{wall} v. L 63 μm	Transitional Disks Only	31.0%	23.6%	24.5%	Not Correlated	-1.65 ± 0.18	0.07 ± 0.04

NOTE.—P is the probability that the correlation between the two listed parameters is obtained by chance; low P values indicate a correlation. The different statistical tests used are: (1) Cox Hazard; (2) Kendall Tau; (3) Spearman Rho. If the average of the three statistical tests is less than 5%, they are listed as "correlated," in boldface. A linear regression (using the EM method) was performed for all combinations, fitting the log of the quantities listed, where the first parameter listed for each pair is the independent variable. If no correlation is detected, the linear regression may not be significant.

TABLE 7
SUBSAMPLE STATISTICAL DIFFERENCE TESTS

Parameter	Subsamples Being Compared	Statistical Difference Tests P(1)	P(2)	P(3)	P(4)	P(5)	Different?
L [OI] 63 μm	Transitional vs. Full Disks	98.4%	98.4%	78.7%	93.8%	94.1%	Not Different
	Transitional vs. Outflow Disks	0.0%	0.0%	0.0%	0.0%	0.0%	**Different**
	Full vs. Outflow Disks	0.0%	0.0%	0.0%	0.0%	0.0%	**Different**
L 63 μm	Transitional vs. Full Disks	9.8%	10.2%	4.8%	9.8%	10.0%	Not Different
	Transitional vs. Outflow Disks	2.1%	1.4%	5.9%	5.9%	—	**Different**
	Full vs. Outflow Disks	0.1%	0.0%	0.0%	0.1%	0.0%	**Different**
L [OI] 63 μm /	Transitional vs. Full Disks	2.2%	1.0%	3.0%	3.1%	1.5%	**Different**
L 63 μm	Transitional vs. Outflow Disks	0.0%	0.0%	0.0%	0.0%	0.0%	**Different**
	Full vs. Outflow Disks	1.8%	1.7%	4.0%	2.3%	2.0%	**Different**
T_{eff}	Transitional vs. Full Disks	78.9%	79.1%	50.1%	50.1%	—	Not Different
	Transitional vs. Outflow Disks	30.8%	31.8%	45.2%	45.2%	—	Not Different
	Full vs. Outflow Disks	11.4%	11.5%	10.3%	10.3%	—	Not Different
L_{bol}	Transitional vs. Full Disks	33.7%	34.3%	76.4%	76.4%	—	Not Different
	Transitional vs. Outflow Disks	2.5%	2.8%	1.7%	1.7%	—	**Different**
	Full vs. Outflow Disks	3.7%	3.4%	0.5%	0.5%	—	**Different**
L_X	Transitional vs. Full Disks	94.3%	94.4%	68.0%	99.0%	1.9%	Not Different
	Transitional vs. Outflow Disks	74.6%	75.1%	97.1%	73.5%	74.9%	Not Different
	Full vs. Outflow Disks	94.8%	94.8%	48.9%	94.7%	96.3%	Not Different
L_{acc}	Transitional vs. Full Disks	68.8%	69.1%	96.2%	68.9%	69.1%	Not Different
	Transitional vs. Outflow Disks	1.9%	1.0%	5.4%	1.9%	1.3%	**Different**
	Full vs. Outflow Disks	1.4%	0.9%	8.5%	1.4%	0.9%	**Different**
$\dot{M}$	Transitional vs. Full Disks	100.0%	100.0%	90.0%	99.7%	99.7%	Not Different
	Transitional vs. Outflow Disks	1.7%	0.8%	4.1%	1.6%	1.0%	**Different**
	Full vs. Outflow Disks	1.9%	1.3%	5.2%	2.0%	1.5%	**Different**
m_{disk}	Transitional vs. Full Disks	59.6%	59.8%	42.6%	53.6%	54.5%	Not Different
	Transitional vs. Outflow Disks	50.7%	50.5%	50.7%	48.3%	48.7%	**Different**
	Full vs. Outflow Disks	75.4%	75.4%	99.8%	75.4%	75.3%	**Different**

NOTE.—P is the probability that the parameter being compared between two subsamples is drawn from the same parent distribution; low P values indicate that two subsamples are different. The different statistical tests are: (1) Gehan generalized Wilcoxon test (with permuation variance); (2) Gehan generalized Wilcoxon test (with hypergeometric variance); (3) logrank test; (4) Peto & Peto generalized Wilcoxon test; (5) Peto & Prentice generalized Wilcoxon test. If the average of the five statistical tests is less than 5%, they are listed as "different," in boldface.

TABLE 8
MEAN PARAMETER VALUES

Parameter	Subsample	Kaplan-Meier Estimator Mean ± Standard Deviation
L [OI] 63 μm	Transitional Disks	-5.12 ± 0.07 log $L_\odot$
	Full Disks	-5.09 ± 0.07 log $L_\odot$
	Outflow Disks	-3.89 ± 0.22 log $L_\odot$
L 63 μm	Transitional Disks	-1.45 ± 0.08 log $L_\odot$
	Full Disks	-1.86 ± 0.17 log $L_\odot$
	Outflow Disks	-0.91 ± 0.20 log $L_\odot$
log(L [OI] 63 μm / L 63 μm)	Transitional Disks	-3.71 ± 0.05
	Full Disks	-3.39 ± 0.08
	Outflow Disks	-2.99 ± 0.10
T_{eff}	Transitional Disks	4066 ± 650 K
	Full Disks	3976 ± 399 K
	Outflow Disks	4299 ± 534 K
L_{bol}	Transitional Disks	-0.43 ± 0.12 log $L_\odot$
	Full Disks	-0.34 ± 0.05 log $L_\odot$
	Outflow Disks	0.13 ± 0.17 log $L_\odot$
L_X	Transitional Disks	-3.89 ± 0.18 log $L_\odot$
	Full Disks	-3.91 ± 0.11 log $L_\odot$
	Outflow Disks	-3.78 ± 0.21 log $L_\odot$
L_{acc}	Transitional Disks	-1.51 ± 0.22 log $L_\odot$
	Full Disks	-1.39 ± 0.16 log $L_\odot$
	Outflow Disks	-0.34 ± 0.32 log $L_\odot$
$\dot{M}$	Transitional Disks	-8.60 ± 0.17 log $M_\odot$/yr
	Full Disks	-8.42 ± 0.18 log $M_\odot$/yr
	Outflow Disks	-7.39 ± 0.36 log $M_\odot$/yr
m_{disk}	Transitional Disks	10.38 ± 3.09 $M_{Jupiter}$
	Full Disks	12.21 ± 3.19 $M_{Jupiter}$
	Outflow Disks	18.10 ± 6.25 $M_{Jupiter}$

NOTE.—The Kaplan-Meier estimator provides an estimate of the mean and standard deviation of the quantity measured, while taking data censoring into account. See LaValley, Isobe, & Feigelson, 1990 for more.